Science Bulletin xxx (xxxx) xxx

Contents lists available at ScienceDirect

Science Bulletin

journal homepage: www.elsevier.com/locate/scib

News & Views

Storms dominate the erosion of the Yangtze Delta and southward sediment transport

Shilun Yang [a,*], Tjeerd J. Bouma [b], Kehui Xu [c,d], Benwei Shi [a], Haifei Yang [a], Wenxiang Zhang [a], Xiangxin Luo [e], Peng Li [f], Yuanguang Huang [a], Min Tian [a], Leicheng Guo [a], Zhijun Dai [a]

[a] State Key Laboratory of Estuarine and Coastal Research, East China Normal University, Shanghai 200241, China
[b] Department of Estuarine and Delta Systems, Royal Netherlands Institute for Sea Research Utrecht University, Yerseke AC 4400, the Netherlands
[c] Department of Oceanography and Coastal Sciences, Louisiana State University, Baton Rouge LA 70803, USA
[d] Coastal Studies Institute, Louisiana State University, Baton Rouge LA 70803, USA
[e] School of Ocean Engineering and Technology, Sun Yat-sen University, Guangzhou 510275, China
[f] East China Sea Centre of Standard and Metrology, State Oceanic Administration of China, Shanghai 201306, China

Densely populated coasts are vulnerable to storm damage. Episodic storm-induced redistribution of coastal sediment is known to have major geological and ecological implications [1,2], but little is known about storm-driven delta erosion and longshore sediment transport. The Yangtze (Changjiang) Delta and Zhejiang–Fujian coasts (Fig. S1 online) are among the world's largest coastal depositional systems, and play an important role in supporting China's socioeconomic development [3,4]. Previous studies have suggested that East Asian winter monsoon wind is the key factor driving southward sediment transport from the Yangtze Delta, creating a 1000-km-long mud wedge on the inner shelf of the East China Sea. Summer (flood season) wind waves are relatively weak and sediments from the Yangtze River are deposited in the delta area, while in winter the northerly monsoon winds drive strong waves and longshore currents, leading to sediment resuspension and removal from the delta [5–7]. However, the role of storms in Yangtze Delta erosion and southward sediment transport has received little attention. Here, we find that episodic storms occurring not only in winter but also in other seasons contribute most to the delta erosion and southward sediment transport.

We defined a fair weather as wind speed $\leq$ 5.4 m/s, storm weather as a wind speed $\geq$ 10.8 m/s, a storm event as a storm wind period $\geq$ 6 h, and a major storm event as a storm period $\geq$ 2 d (see Methods in the Supplementary materials online). On the Yangtze Delta, longshore wind is dominated by southward winds, particular for storm winds of which 86% are southward (Table S1 online). In the Northern Hemisphere, storm winds derived from polar outbreaks are southward. Likewise, typhoon-driven storm winds are usually southward, with typhoons commonly being formed over the ocean southeast of the Yangtze Delta and rotating counterclockwise as they approach and commonly move northward on the east side of the Yangtze Delta (e.g., Malakas track in Fig. S1a online). Storm winds contribute >30% of the total net southward wind component, although storm winds occur on only ~5% of days per year (Tables S1 and S2 online).

Our observations indicate that wind speed and wave height during storm events were respectively 2–4 and 3–5 times higher than during fair weather (Fig. 1a, b, Figs. S2–S4, and Table S3 online). Wave energy is proportional to the square of wave height [8], so wave energy during storm events is an order of magnitude higher than during fair weather. Storm surges enhance sediment resuspension in shallow waters and initiate sediment resuspension in deeper waters where the seabed is not disturbed during fair weather.

For example, during Typhoon Malakas in 2016, the daily average surficial suspended sediment concentration (SSC) at Station A (7 m depth; Fig. S1b online) reached a maximum of 1.45 kg/m^3 on 19 September, 34 times that during fair weather one week earlier (0.043 kg/m^3 on 11–12 September) (Fig. S3f online). Under the assumption of no storm impact, and based on the power-law relationship between daily average SSC and tidal range in fair weather (Fig. S5d online), the maximum SSC increase on 19 September due to increased tidal effect alone would have been 0.676 kg/m^3 (Fig. S3f online). Therefore, ~45% of the increased SSC from 11–12 to 19 September was due to the increased tidal range, while ~55% was attributable to storm impact. Thus, storm impact alone increased the SSC by 18 times. At Station B (20 m depth; Fig. S1b online), the mean SSC on 19 September (0.432 kg/m^3) was 55 times that on 11–12 September (0.0078 kg/m^3) (Fig. S4g, h online). Thus, ~30% of the SSC increase (16 times) from 11–12 to 19 September resulted from the increased tidal range, while ~70% (38 times) resulted from storm-induced sediment resuspension.

To better understand sediment resuspension during Typhoon Malakas, we compared the SSC among phases. During Phase 1 (four tidal cycles), when both waves and currents were weak, the SSC was low. During Phase 2 (eight tidal cycles), the SSC increased with wave height and current velocity due to the approaching typhoon and the transition from neap to spring tide. During Phase 3 (five tidal cycles), the SSC further increased as both the wave height and current velocity reached their maxima (Table S3 online). From Phase 1 to Phase 3, the SSC at stations A and B increased by 22 and 35 times, respectively. Based on the relationship between SSC and

* Corresponding author.
E-mail address: slyang@sklec.ecnu.edu.cn (S. Yang).

https://doi.org/10.1016/j.scib.2023.03.005

Please cite this article as: S. Yang, T.J. Bouma, K. Xu et al., Storms dominate the erosion of the Yangtze Delta and southward sediment transport, Science Bulletin, https://doi.org/10.1016/j.scib.2023.03.005

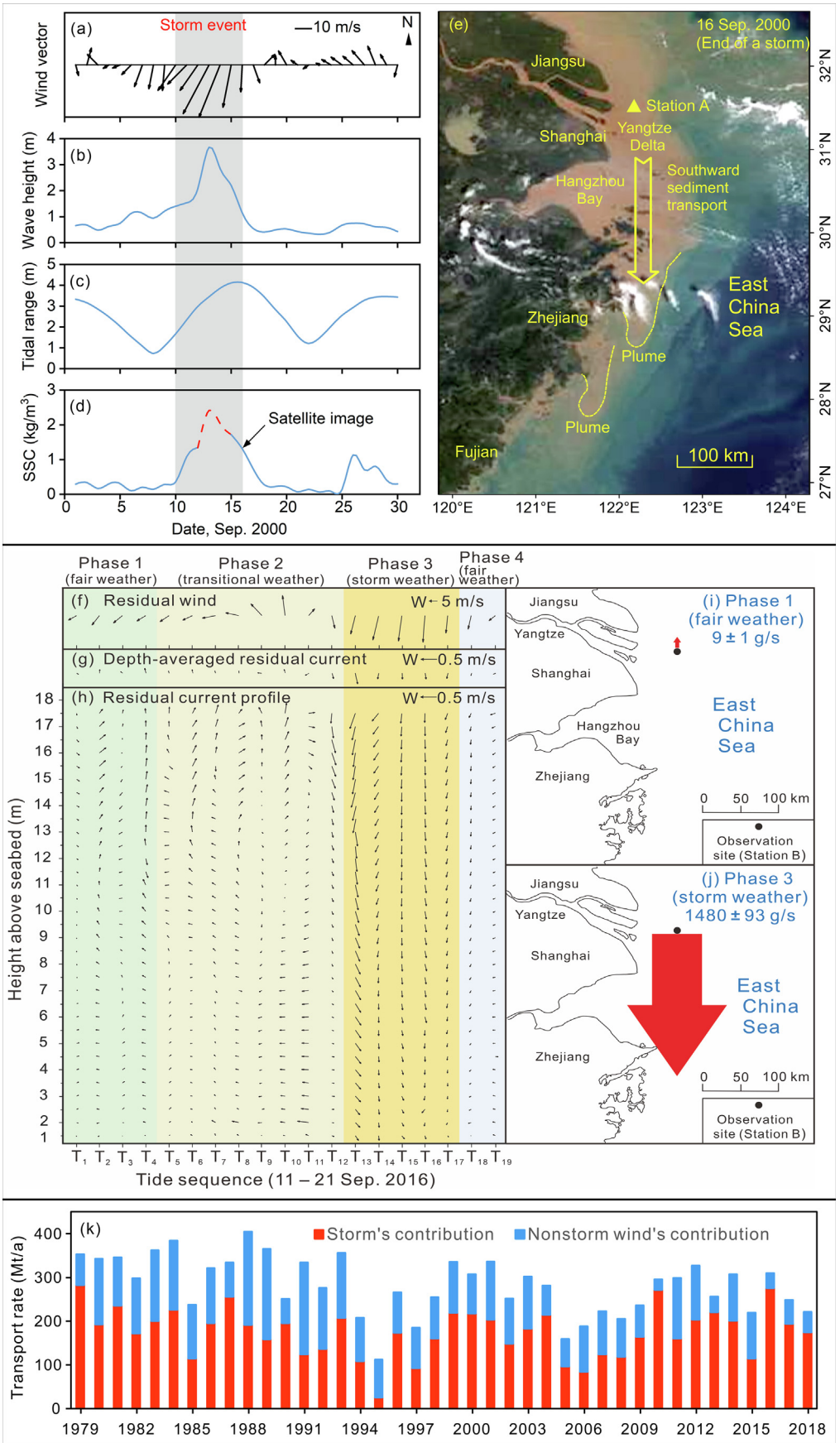
(a)
Storm event
—10 m/s
N
Wind vector
(b)
Wave height (m)
(c)
Tidal range (m)
(d)
SSC (kg/m³)
Satellite image
Date, Sep. 2000
(e)
16 Sep. 2000
(End of a storm)
Jiangsu
Station A
Shanghai
Yangtze
Delta
Hangzhou
Bay
Southward
sediment
transport
East
China
Sea
Zhejiang
Plume
Plume
Fujian
100 km
120°E
121°E
122°E
123°E
124°E
32°N
31°N
30°N
29°N
28°N
27°N
Phase 1
(fair weather)
Phase 2
(transitional weather)
Phase 3
(storm weather)
Phase 4
(fair weather)
(f) Residual wind
W←5 m/s
(g) Depth-averaged residual current
W—0.5 m/s
(h) Residual current profile
W—0.5 m/s
Height above seabed (m)
Tide sequence (11 – 21 Sep. 2016)
(i) Phase 1
(fair weather)
9 ± 1 g/s
Observation
site (Station B)
(j) Phase 3
(storm weather)
1480 ± 93 g/s
(k)
Storm's contribution
Nonstorm wind's contribution
Transport rate (Mt/a)

tidal range in fair weather (Fig. S5d online), 68% of the SSC increase at Station A and 46% at Station B from Phase 1 to Phase 3 is attributed to the increased tidal effect. It follows that 32% of the SSC increase at Station A and 54% at Station B can be attributed to storm impact.

Storm-induced sediment resuspension results in an expansion of the turbid zone toward deeper waters. A satellite image taken near the end of a storm event associated with Typhoon Sonamu shows an ~80-km-wide turbid zone in the offshore subaqueous Yangtze Delta (Fig. 1e), which is ~40 km wide under normal weather conditions [9]. Considering that wind speed, wave height, and SSC during the strongest period of the storm (2–3 d before the time when the satellite image was obtained) were much higher than when the image was taken (Fig. 1a, b, d), the turbid zone in the offshore subaqueous Yangtze Delta during the strongest period of the storm would have been wider than that shown in the image.

Southward storm winds drive southward residual currents in the offshore subaqueous Yangtze Delta. Under fair-weather conditions prior to Typhoon Malakas, residual currents of individual tidal cycles had low velocities and varied directions that were inconsistent with residual wind directions. However, during the typhoon event, the residual current velocities were increased markedly, and their directions were consistent with the residual wind direction in both vertical profiles and time series (Fig. 1f–h and Table S4 online). During fair weather, when the residual wind speed and direction were 5.3 m/s and 59°, the depth-averaged residual current velocity and direction were 0.07 m/s and 354° (the flow direction is the direction of on-going flow), respectively. During the storm event, the residual wind speed and direction were 10.1 m/s and 12°, and the depth-averaged residual current velocity and direction were 0.32 m/s and 180°, respectively (Table S5 online).

We estimated the residual sediment transport rate per unit width of cross-section as the product of water depth, depth-averaged residual current velocity, and depth-averaged SSC. The residual sediment transport rate per meter width of the water column at Station B during Typhoon Malakas was 1480 ± 93 g/s (see Methods in the Supplementary materials online for uncertainties) (direction of 180°), far exceeding the fair-weather value of 9 ± 0.7 g/s (direction of 354°) (Fig. 1i, j and Table S5 online). We also found increased median sizes of suspended and bottom sediments during and immediately after the typhoon event, suggesting storm-induced southward transport of coarser-grained sediments. To estimate the residual sediment transport rate through the cross-shore profile, we first quantified the cross-shore changes in SSC (Fig. S6 online). The depth-averaged residual current velocity at Station B was then used to represent the mean residual velocity in the cross-shore profile, considering that (1) the offshore subaqueous delta is open (Fig. S1a online) and cross-shore changes in wind speed and direction during the storm were negligible (Fig. S7 online), (2) the coastal slope is very gentle (gradient < 0.03%) and smooth (Fig. S1c online), and (3) Station B is located centrally in the offshore subaqueous delta (Fig. S1b online). The water depth for each unit width was then calculated from Fig. S1c (online). Finally, the total longshore sediment transport flux during the storm event was estimated as the product of the residual sediment transport rate through the cross-shore profile and the duration of the storm.

We found that ~63 ± 4.1 Mt of sediment was transported southward from the offshore subaqueous delta during the Malakas event (Table S6 online). This is 126 times the sediment supplied by the Yangtze River during the event (0.5 Mt) and indicates that 99% of the southward sediment transport was derived from delta erosion. Considering that the offshore subaqueous Yangtze Delta covers an area of ~10,000 km^2 (Fig. S1b online) and the mean dry bulk density of Yangtze River sediment is 1.3 g/cm^3 [4], the mean erosion depth during the Malakas event was ~5 ± 0.3 mm. Our optimal estimate of the storm-induced southward sediment transport from the Yangtze Delta during 2016 was 275 ± 54 Mt, or 89% of the total sediment transport. Optimal estimates of storm-induced annual fluxes of southward sediment transport from the delta over the past 40 years have varied between 25 ± 4.5 Mt in 1995 and 282 ± 55 Mt in 1979, with an average of 175 ± 69 Mt/a. The marked interannual changes in storm-induced southward sediment transport from the Yangtze Delta (Table S7 online) reflect the impact of climatic variability. On average, 52% of the storm-induced annual net southward sediment transport has occurred in winter, 39% has occurred in autumn, and 9% has occurred in spring (Table S8 online). The storm contribution to total sediment transport ranges from 23% in 1995 to 92% in 2010, with an average of 62% (Fig. 1k and Table S7 online).

Prior to the closure of the Three Gorges Dam (TGD) (1979–2002), Yangtze sediment discharge to the sea was 379 ± 79 Mt/a, while our estimate of southward sediment transport from the Yangtze Delta was 300 ± 90 Mt/a with 176 ± 69 Mt/a being contributed by storms. After the TGD closure (2003–2018), the Yangtze sediment discharge rate was 133 ± 42 Mt/a, while our estimate of sediment transport from the Yangtze Delta was 254 ± 67 Mt/a with 175 ± 69 Mt/a being contributed by storms (Table S7 online). Thus, the Yangtze Delta underwent a transition from pre-TGD accretion to post-TGD erosion, which is in agreement with measured bathymetric changes [10]. The annual storm-driven transport exceeded the post-TGD discharge and was less than the pre-TGD discharge, thus causing the Yangtze Delta transition.

We developed a conceptual model of the fate of Yangtze-derived sediments. In fair weather, when waves are low and residual longshore currents are weak, fluvial sediments from the Yangtze tend to be deposited on the offshore subaqueous delta. However, in stormy weather, when wave energy and bottom perturbation are greatly increased and southward longshore currents are stronger, previously deposited sediments are resuspended and transported southward (Fig. S8 online). The southward transport distance during a storm event is typically <100 km. For example, the distance of southward sediment transport during the Malakas event was ~70 km, based on the duration (2.6 d) and mean residual flow velocity during the storm period (0.32 m/s) (Table S5 online).

Our optimal estimate of the mean rate of southward sediment transport from the Yangtze Delta over the past four decades (280 ± 85 Mt/a) is consistent with results of previous studies based on observations and sediment budgets [7,11]. The sediment transport is generally dominated by storm-induced resuspension and

Fig. 1. Storm-induced changes in hydrodynamics and sediment transport. (a–d) Daily average wind vector, significant wave height, tidal range, and suspended sediment concentration (SSC) at Station A. (e) Satellite image at the end of a storm showing turbid zone and southward sediment plums. (f–h) Tidal-cycle residual wind vector, depth-averaged current, and current profile at Station B. (i, j) Residual sediment transport rates and direction per meter width of the water column at Station B in fair weather and storm event. (k) Storm's and nonstorm wind's contributions to annual net southward sediment transport from the Yangtze Delta. Note: the broken line in (d) is an estimate of missing SSCs for 12–15 September, when sediment-sampling efforts failed because of dangerous storm winds and surges. The estimate was based on a binary regression between SSC and wave height and tidal range in the other 26 d in September (R^2 = 0.65, P < 0.001).

longshore currents, even though transport driven by southward nonstorm winds of the winter monsoon may exceed storm-induced transport in some individual years when storm events are rare. Storm-induced southward sediment transport is not limited to winter or the winter monsoon period but may occur in most seasons. Marked increases in SSC and surficial sediment grain size found immediately after typhoons in the mud wedge also suggest storm-induced sediment resuspension and redistribution [12,13]. Our results differ from those of previous studies that attributed southward sediment transport to longshore currents driven by the winter monsoon [5,7]. Our findings highlight the importance of storms in delta erosion and longshore sediment delivery, which is of particular significance considering the projected increase in storm intensity with global warming [14] and the dam-induced decrease in river sediment discharge to the world's coastal seas [15].

Conflict of interest

The authors declare that they have no conflict of interest.

Acknowledgments

This work was supported by the Ministry of Science and Technology of China (2016YFE0133700) and the National Natural Science Foundation of China (42106167 and 42076170).

Appendix A. Supplementary materials

Supplementary materials to this news & views can be found online at https://doi.org/10.1016/j.scib.2023.03.005.

References

[1] Turner RE, Baustian JJ, Swenson EM, et al. Wetland sedimentation from hurricanes Katrina and Rita. Science 2006;314:449–52.
[2] Winterwerp JC, van Kesteren WGM, van Prooijen B, et al. A conceptual framework for shear flow–induced erosion of soft cohesive sediment beds. J Geophys Res 2012;117:C10020.
[3] Liu JP, Xu KH, Li AC, et al. Flux and fate of Yangtze River sediment delivered to the East China Sea. Geomorphology 2007;85:208–24.
[4] Yang SL, Luo XX, Temmerman S, et al. Role of delta-front erosion in sustaining salt marshes under sea-level rise and fluvial sediment decline. Limnol Oceanogr 2020;65:1990–2009.
[5] Shepard FP. Sediments of the continental shelves. Geol Soc Am Bull 1932;43:1017–40.
[6] Milliman JD, Shen HT, Yang ZS, et al. Transport and deposition of river sediment in the Changjiang Estuary and adjacent continental shelf. Cont Shelf Res 1985;4:37–45.
[7] Deng B, Wu H, Yang SL, et al. Longshore suspended sediment transport and its implications for submarine erosion off the Yangtze River Estuary. Estuar Coast Shelf Sci 2017;190:1–10.
[8] Guillou N. Estimating wave energy flux from significant wave height and peak period. Renew Ener 2020;155:1383–93.
[9] Tang R, Shen F, Ge J, et al. Investigating typhoon impact on SSC through hourly satellite and real-time field observations: a case study of the Yangtze Estuary. Cont Shelf Res 2021;224:104475.
[10] Luan HL, Ding PX, Yang SL, et al. Accretion-erosion conversion in the subaqueous Yangtze Delta in response to fluvial sediment decline. Geomorphology 2021;382:107682.
[11] Guo X, Fan D, Zheng S, et al. Revisited sediment budget with latest bathymetric data in the highly altered Yangtze (Changjiang) Estuary. Geomorphology 2021;391:107873.
[12] Li Y, Li D, Fang J, et al. Impact of Typhoon Morakot on suspended matter size distributions on the East China Sea inner shelf. Cont Shelf Res 2015;101:47–58.
[13] Li Y, Li H, Qiao L, et al. Storm deposition layer on the Fujian coast generated by Typhoon Saola. Sci Rep 2012;5:14904.
[14] Sobel AH, Camargo SJ, Hall TM, et al. Human influence on tropical cyclone intensity. Science 2016;353:242–6.
[15] Li L, Ni J, Chang F, et al. Global trends in water and sediment fluxes of the world's large rivers. Sci Bull 2020;65:62–9.

Shilun Yang is a professor of the State Key Laboratory of Estuarine and Coastal Research, East China Normal University. His research fields are geomorphology, hydrology, and sediment dynamics, with particular interest in coastal responses to storm impact and human-induced fluvial sediment decline.

The Supplementary Materials are attached below

Supplementary materials

1. Regional setting

The Yangtze River, which at 6,400 km long is one of the world's longest rivers, has a drainage area of 1.8 million km^2 [1], discharges 900 km^3/a of water, and (prior to dam construction) discharged 500 Mt/a (Mt: million tons) of sediment; The Yangtze Catchment is currently home to 450 million people [2]. The Yangtze Delta is among the world's largest deltas in terms of size, ecosystem, population, and economy [3]. Shanghai, currently the largest harbor city in the world, lies at the mouth of this river. The offshore subaqueous Yangtze Delta has an area of ~10,000 km^2 (Fig. S1b). The loose sediment in the offshore subaqueous delta is composed mainly of silt, clay, and very fine sand, which are easily resuspended by waves and currents [4]. The median size of the suspended sediments is 3–7 μm [5]. The tides in this delta are semidiurnal with a diurnal inequality. The tidal range in the offshore subaqueous delta is 2.7 m on average, but can exceed 4.0 m during spring tides [3]. The tidal flow in the offshore subaqueous delta is rotating [6]. Located on the exposed northwestern Pacific coast, the Yangtze Delta is frequently affected by typhoons and cold fronts. Annually, more than ten major storms (typhoons and polar outbreaks) affect the Yangtze Delta. Between 1949 and 2020, the number of typhoons passing across the East China Sea reached 524, which was 27% of the total number of typhoons formed in the Western Pacific Ocean [7]. Most of these typhoons affected the Yangtze Delta [8, 9–11]. The typhoon-generated storms affecting the Yangtze Delta occur mainly in summer and autumn [9–11]. Climate models project an increasing Typhoon intensity in the 21st century over the Western North Pacific [12]. The significant wave height at Sheshan Station (30 km offshore) is <1.0 m during fair weather but increases to several meters during storm events [10]. The suspended sediment concentrations (SSCs) in the offshore subaqueous delta range from <0.1 to > 2.0 kg/m^3, increasing from neap to spring tides, from fair to stormy weather, from surface to near-bed water layers, and from offshore to the mouth-bar areas [13]. Furthermore, the offshore subaqueous Yangtze Delta is characterized by a southward longshore current (Fig. S1a), which is believed to be driven mainly by the East Asian winter monsoon [14–16].

In the administrative division, Zhejiang and Shanghai border the middle part of the north bank of Hangzhou Bay (Fig. 1e). In other words, the Zhejiang Coast is located just south of the Yangtze Delta. Fujian is located south of Zhejiang (Fig. S1a). Since the mid Holocene, a vast longshore mud wedge has formed in the inner shelf of the East China Sea along the macrotidal coasts of Zhejiang and Fujian provinces, southeastern China, mainly as a result of southward transport of sediment from the Yangtze Delta [17,6,18]. The mud wedge is approximately 1,000 km in length, 100 km in width, and 40 m in thickness (Fig. 1a) [17]. The sediments of this mud wedge are dominated by silts and clays, with a gradual fining trend from north to south [1]. This mud wedge is even larger than the Yangtze Delta in terms of both area and volume [17,19], suggesting that more than half of the sediments from the Yangtze River have been transported southward to build the longshore mud wedge. The mud wedge extends into coastal embayments and leads to the formation of tidal wetlands. Historical reclamation of tidal wetlands in these embayments has produced a large amount of new land and promoted socioeconomic development. For example, the reclamation rate in Zhejiang Province during the past decades reached 37 km^2/a [20], markedly exceeding the contemporaneous reclamation rate in the Yangtze Delta (20 km^2/a) [21].

2. Methods

2.1. Field observation

We conducted field observations at Stations A (122.248° E; 31.432° N) and B (122.440° E; 31.401° N) in the offshore subaqueous delta (Fig S1b) during different periods in 2016 to sample the water and measure hydrodynamics

and turbidity before, during, and after storms. Station A is 1 m off the fore-end of an exposed wharf built on the landward side of a small island (Sheshan, area 0.04 km^2), where the time-averaged water depth is 7 m. Station B, where the time-averaged water depth is 20 m, is ~20 km more seaward than Station A.

At Station A, 600 ml of surface water was sampled twice daily (08:00 and 14:00). The water samples were filtered through preweighed 0.45-μm filters, rinsed and dried at 45°C for 48 h, and then weighed. The SSC was calculated as the ratio of dry suspended sediment weight to the filtered water volume. Wind speeds and directions 10 m above the sea surface were measured using an XFY3 Swirl Wind Sensor (National Marine Technology Centre, Tianjin, China). Significant wave heights and mean wave periods were measured using an SBY1-1 pressure wave sensor (Institute of Oceanographic Instrumentation, Qingdao, China) fixed on a buoy next to the station.

At Station B, hydrodynamics and turbidities were synchronously measured during 11–21 September 2016 using instruments fixed on a tripod. Significant wave heights, mean wave periods, current profiles, and water-depth changes were measured using an acoustic Doppler current profiler (ADCPWaves; Teledyne RD Instruments, Inc., San Diego, USA). The ADCPWAVES sensor was 0.5 m above the seabed and facing upward, with a blind spot of 0.7 m and a 0.5 m layer interval. Turbidities and water-depth changes were measured at 1-min intervals using two optical backscatter sensors (OBS; OBS-3A, Campbell Scientific, Inc., Salt Lake City, USA) fixed at 0.5 m and 1.2 m above the seabed; the water-depth changes measured by the two instruments were highly consistent (<1% difference).

2.2. Data mining

Data on typhoon tracks and maximum wind speeds near the typhoon centers in 2016 were obtained from the National Meteorological Center of China (http://www.nmc.cn/). In addition, predictions of the wind speed, wind direction, significant wave height, and mean wave period (6-h temporal resolution) were obtained from the European Centre for Medium-Range Weather Forecasts (ECMWF; https://www.ecmwf.int/). The longitudinal and latitudinal resolutions of the ECMWF predictions are 0.125° × 0.125°. We obtained ECMWF data for points as close to the two stations as possible, designating these locations Station A′ (122.250° E; 31.375° N) and Station B′ (122.500° E; 31.375° N), which are the closest grid points to Station A and Station B, respectively. The astronomical tide data at Station A were obtained from the East China Sea Branch, State Oceanic Administration of China. Data on the 2016 daily water discharge and SSC of the Yangtze River measured at Datong Station which is located at the tidal limit (Fig. S1a) were obtained from the Yangtze Water Resource Committee. A satellite image of the turbid zone along the inner shelf of the East China Sea was obtained from the United States Geological Survey (USGS; https://www.usgs.gov/core-science-systems/nli/landsat)

2.3. Definitions

Here, we use the term "storm" to refer to an extreme weather event (typhoon or polar outbreak) during which the wind speed is significantly higher than that during fair weather [22–23]. Wind speed is classically divided into thirteen units (Beaufort scales 0–12) [24]. Considering the wind-speed characteristics in the study area and taking into account the customary rule on wind scales [24], we defined fair wind as wind scales 0–3 (average wind speed ≤ 5.4 m/s), moderate wind as scales 4–5 (average wind speed of 5.5–10.7 m/s), nonstorm wind as wind scales 0–5 (average wind speed < 10.8 m/s), and storm wind as wind scales ≥ 6 (average wind speed ≥ 10.8 m/s). In addition, we defined a storm event as a storm wind period ≥ 6 hours and a period-averaged wind speed ≥ 10 m/s and a major storm event as a storm period ≥ 2 days.

The typhoon force index (TFI) is defined as the ratio of the maximum wind speed near the typhoon center to the distance between the typhoon center and the point of interest (here, one of the two observation stations in the Yangtze Delta). Because the units of wind speed and distance are m/s and km, respectively, the unit of TFI is 10^{-3}/s. The TFI is a useful value for reflecting the potential impact of a typhoon, even though the unit of TFI has no physical meaning.

The net wind component is defined as the algebraic sum of wind components. The cumulative force of a wind

component is defined as the sum of the products of the wind component and its duration. For example, given a 6-h-average eastward wind component of 5 m/s and a 6-h-average eastward wind component of −4 m/s, the cumulative force of the eastward wind component in the 12-h period is 5 m/s × 6 h × 3,600 s/h – 4 m/s × 6 h × 3,600 s/h = 21,600 m. We defined a tidal cycle as the duration between two successive low tides.

2.4. Testing for reliability of the ECMWF-predicted wind and wave data

We created scatter diagrams and performed statistical analyses to examine the correlations between variables. The ECMWF-predicted wind speeds and directions were similar between Points A′ and B′ (R^2 = 0.99, p < 0.001; Fig. S7). The ECMWF predictions were similar to our observations obtained nearby (R^2 = 0.85–0.91, p < 0.001 for wind speed, Fig. S9; R^2 = 0.87–0.88, p < 0.001 for wave height in fair-weather and storm conditions, Fig S10a–b; and R^2 = 0.63–0.75, p < 0.001 for wave height in fair-weather, storm, and poststorm conditions, Fig. S10 c–d). Close correlations existed between the ECMWF-predicted mean wave periods at Points A′ and B′ (R^2 = 0.95, p < 0.001; Fig. S11a) and the measured significant and mean wave periods at Station A′ (R^2 = 0.99, p < 0.001; Fig. S11b). Therefore, we used the ECMWF predictions and correlation equations to investigate the temporal trends of wind speed and significant wave height and wave period when measured data were missing. Hence, regression equations were employed to simulate the wind and wave data for the remainder of 2016.

2.5. Calibration of turbidity and conversion to SSC

In situ turbidity data obtained from the OBSs at Station B were converted into SSC data via regression equations with close correlations (R^2 = 0.99, p < 0.001) calibrated using the water and sediment samples collected in the field (Fig. S12). Specifically, the sediment was fully mixed with water in a barrel (0.6 m diameter) to generate turbidity. The turbidity was measured using the two OBS sensors that were used in the field, and the turbid water was sampled. We changed the turbidity by increasing water or sediment into the barrel. By doing so, we obtained a series of SSC and turbidity data (from low to high levels). The water samples were filtered, rinsed, dried, and weighed, and SSC values were calculated, as described above. Subsequently, the SSC and turbidity datasets from indoor calibrations were used to establish the correlations in Fig. S12.

2.6. Differentiating tide- and storm-induced sediment resuspension

To differentiate tide- and storm-induced SSC changes during storm events, we found a significant correlation between the SSC and tidal range under fair-weather conditions with a 1-day lag in the SSC behind the tidal range (R^2 = 0.8, p < 0.001; Fig. S5). We subsequently employed this regression relationship and used the tidal ranges measured during the storm events to predict tide-generated SSC changes alone. The differences between the SSC measurements and the SSC predictions from this regression relationship reflect the storm-induced SSC changes.

2.7. Calculation of current profiles

The water depths measured at Station B ranged from 17.7 to 22.3 m. Because the ADCP sensor was 0.5 m above the seabed and the blind spot of this sensor was 0.7 m, the currents in 33 layers between 1.2 and 17.7 m above the seabed (each layer was 0.5 m thick) were completely measured, whereas the currents in the upper layers were only partly measured. As a result, we used only the measurements from the lowest 33 layers to calculate the current profiles, and the currents within 1.2 m above the seabed were estimated using an extrapolation method.

2.8. Calculation of SSC profiles

Based on 402 individual SSC profiles measured at various stations throughout the offshore subaqueous Yangtze Delta during various seasons and tidal cycles, Liu et al. (2014) found an average relative SSC profile (i.e., SSC changes with relative water height), in which the SSC showed an exponentially increasing trend with depth (R^2 = 0.99) [8]. The relative vertical change in SSC obtained in that study is in good agreement with the finding of Whitehouse et al. (2000) for estuarine SSC [25], suggesting that their relative vertical change is overall typical and can be used to simulate SSC

profiles. We utilized the relative vertical changes in SSC and the measured SSCs at 0.5 and 1.2 m above the seabed at Station B to simulate the SSC profiles during fair and stormy weather. The results of the two sets of simulations were generally consistent. To minimize the error in simulation, we calculated the average of the two sets of SSC profiles. During the weakening and immediately after the disappearance of Typhoon Malakas, sediments in the upper water column largely settled to the near-bed layer; therefore, the near-bed SSCs (i.e., the SSCs 0.5 and 1.2 m above the seabed) were significantly increased rather than decreased, distorting the SSC profile. To describe these distorted SSC profiles, we assumed that the poststorm surficial SSC decreased to the prestorm level with hydrodynamics similar to those in the poststorm period. The predicted surficial SSCs, combined with the measured SSCs at 0.5 and 1.2 m above the seabed, yielded simplified poststorm SSC profiles. Subsequently, we simulated the tidal cycle-averaged SSC profiles using a power regression approach ($R^2 = 0.99$) and calculated the tidal cycle-averaged SSCs for the rest of the layers.

2.9. Calculation of residual wind, current, and sediment transport

Residual wind speed and direction, residual current velocity and direction, and residual sediment transport rate and direction were calculated using a vector approach for eastward (westward) and northward (southward) components. To minimize the influence of tidal flows on the calculation of residual current, we employed the tidal cycle as the elementary unit of calculation for the residual current velocity and direction, because the net water movement induced by tidal flows during the tidal cycle is expected to be minimal.

2.10. Calculation of wavelength

We calculated wavelengths using equations for Airy wave theory:

$$L_{deep} = gT^2/2\pi \ (h/L > 0.25) \quad (1)$$

for deep-water conditions,

$$L_{transitional} = (gT^2/2\pi) \ (\tanh[2\pi h/L]) \ (0.25 > h/L > 0.05) \quad (2)$$

for transitional water depth, and

$$L_{shallow} = T \ (gh)^{0.5} \ (h/L < 0.05) \quad (3)$$

for shallow-water conditions, where L is the wavelength, $g = 9.81$ m/s^2, T is the wave period, $\pi = 3.1416$, and h is the water depth [26].

2.11. Estimate of annual net southward sediment transport

~57% (the average from Stations A and B) of the SSC increase during the Malakas event was attributable to sediment resuspension resulting from the increased tidal range from neap (Phase 1) to spring tides (Phase 3). If Typhoon Malakas had occurred during a mean tide (tidal range 2.7 m), rather than a spring tide (tidal range 4.1 m), the tidal effect on SSC would have decreased by 83%, based on the relationship between SSC and the tidal range (Fig. S5d). Thus, the SSC during the Malakas event under a mean tidal condition would have been ~47% lower than the observed SSC. In total, the amount of sediment transported southward from the Yangtze Delta during Typhoon Malakas can be reduced from 63 to 33 Mt for mean tidal conditions. We identified four other major storm events in 2016 that were similar to Malakas in terms of duration and southward wind component. Thus, the longshore sediment transport from the Yangtze Delta associated with these five major storm events (including Malakas) would have been around 165 Mt. These five major storms contributed ~45% of the total southward wind component generated by the twenty-nine storms that affected the Yangtze Delta during 2016. Considering that a persistently blowing duration is more effective in the generation of waves and residual currents than several discontinuous short blowing durations under equal wind directions, wind speeds, and cumulative wind durations [27], the southward sediment transport induced by the twenty-four minor storm events was most probably less than that resulting from the five major storm events. In addition, 4% of the southward storm component was neutralized by the northward storm component in 2016 (Table S1). Thus, we roughly estimate that the total amount of southward sediment transport from the offshore subaqueous

Yangtze Delta driven by storm events in 2016 was approximately 250–300 Mt/a. The rationality of this estimate of annual storm-induced residual sediment transport based on extension from a typhoon event is that the mechanisms of different storms (typhoon or polar outbreak) affecting longshore sediment transport are similar. That is, the southward storm winds not only increase wave power and sediment resuspension (thereby increasing SSC) but also drive strong longshore currents. The ratios of the net southward storm wind force in 2016 to the net southward storm wind force in other years were employed in estimating the storm-induced annual southward sediment transport in other years. Estimate of the nonstorm wind-induced annual southward sediment transports is described in the note below Table S7.

2.12. Uncertainty estimate

In this study, uncertainties in data and estimations include measurement errors, calculation errors, and standard deviations from average values. According to the instrument instruction manuals, the flow velocity error measured using ADCPWAVES is ±0.25%, and the turbidity error measured using OBS-3A is ±0.1 NTU for turbidities of 0–100 NTU, ±1 NTU for turbidities of 100–500 NTU, and ±5 NTU for turbidities of 500–4000 NTU. Our measured turbidities range from 3 to 3950 NTU, and are 185 NTU on average. That is, the errors of the measured turbidities are between 0.13% and 3% and are 0.5% on average. Our estimates of tidal cycle- and depth-averaged SSC range from 4 to 422 mg/l. The square of the correlation coefficient (R^2) between SSC and turbidity is 0.99 (Fig. S12). In this study, we employed the mean SSC profile by Liu et al. (2014) to reconstruct tidal cycle-averaged and phase-averaged (two to eight tidal cycles) SSC profiles (see Section 2.8). The R^2 between SSC and relative depth in the mean SSC profile by Liu et al. (2014) is 0.99 [5]. Because the mean SSC profile by Liu et al. (2014) is based on 402 individual SSC profiles measured at various stations throughout the offshore subaqueous Yangtze Delta during various seasons and tidal cycles, we assume that the change in SSC relative to depth shown in their mean SSC profile is applicable in this study. Most importantly, we used the mean SSC profile by Liu et al. (2014) to reconstruct tidal cycle-averaged and phase-averaged SSC profiles (750 individual measurements of near-bed SSC in each tidal cycle) rather than reconstructing any instantaneous individual SSC profile. In the cross-shore profile, the R^2 between the depth-averaged SSC and water depth is also 0.99 (Fig. S6). Based on statistics, an R^2 of 0.99 indicates that the deviations of variables from the trendline are 1%, with 95% confidence [28]. Comprehensively speaking, the combined error of our estimate of the sediment transport rate is most likely less than ~8%. In addition, the uncertainty range of the average of a set of data is calculated using the standard deviation. The average and standard deviation were calculated using Microsoft Excel software. In estimating the uncertainty ranges of residual sediment transport and its influential factors (flow velocity and SSC) during tidal cycles and phases (several tidal cycles), we included errors in measurements and calculations but excluded the standard deviations in time series data (Table S5–S6) because the standard deviations were mainly derived from tide-induced cyclic changes in the influential factors. In estimating the uncertainty ranges of multiyear-averaged annual net sediment transport, however, we included both the errors and standard deviations (Table S7) because the standard deviations reflect the impact of aperiodic wind changes.

3. Reliability and Limitations

Overall, our estimate of the multi-year average southward sediment transport rate from the Yangtze Delta (~280 Mt/a) is consistent with the results of previous studies (210–350 Mt/a) [14–15, 29–31], suggesting that our hypothesis regarding the dominant role of storms in this southward sediment transport is reasonable. However, because of difficulties in field work and inadequate instrumentation, our observations were incomplete. There are two major areas of uncertainty associated with our estimate of storm-driven southward sediment transport. First, the vertical SSC trend described by Liu et al. (2014) is a spatiotemporal average [5], and our use of this trend to predict the vertical SSC distributions at depths of 7 and 20 m in the offshore subaqueous delta is a possible source of error. Second, the stations at depths of 7 and 20 m and the intertidal flat station were some distance apart and not located along a cross-shore

profile, even though the observations were conducted simultaneously. Hence, the cross-shore distribution of longshore sediment transport based on only these three stations is probably somewhat different from the actual distribution. Thus, further work will be needed to verify our findings. Specifically, field observations of hydrodynamics and SSCs should be improved by adding cross-shore transects on the Yangtze Delta and the mud wedge areas, adding observation stations along the cross-shore transect, adding turbidity sensors to the vertical profile, and using research vessels to collect data during storm and nonstorm events in different seasons.

References

[1] Gao JH, Shi Y, Sheng H, et al. Rapid response of the Changjiang (Eangtze) River and East China Sea source-to-sink conveying system to human induced catchment perturbations. Mar Geol 2019; 414: 1–17.

[2] Yang HF, Yang SL, Xu KH, et al. Human impacts on sediment in the Yangtze River: A review and new perspectives. Global Planet Change 2018; 162: 8–17.

[3] Yang SL, Luo XX, Temmerman S, et al. Role of delta-front erosion in sustaining salt marshes under sea-level rise and fluvial sediment decline. Limnol Oceanogr 2020; 65: 1990–2009.

[4] Luo XX, Yang SL, Wang RS, et al. New evidence of Yangtze Delta recession after closing of the three gorges dam. Sci Rep 2017; 7: 41735.

[5] Liu JH, Yang SL, Zhu Q, et al. Controls on suspended sediment concentration profiles in the shallow and turbid Yangtze Estuary. Cont Shelf Res 2014; 90: 96–108.

[6] Guo L, Zhu C, Xie W, et al. Changjiang Delta in the anthropocene: Multi-scale hydro-morphodynamics and management challenges. Earth-Sci Rev 2021; 223: 103850.

[7] Huang, YG. Response of suspended sediment concentration to in Yangtze Estuary and its adjacent seas to reservoir construction and typhoon and its environmental effects. Dissertation for Doctoral Degree. Shanghai: East China Normal University, 2022.

[8] Yang SL, Fan JQ, Shi BW, et al. Remote impacts of typhoons on the hydrodynamics, sediment transport and bed stability of an intertidal wetland in the Yangtze Delta. J Hydrol 2019; 575: 755–766.

[9] Yang SL, Friedrichs CT, Shi Z, et al. Morphological response of tidal marshes, flats and channels of the outer Yangtze River mouth to a major storm. Estuar Coast 2003; 26: 1416–1425.

[10] Fan D, Guo Y, Wang P, et al. Cross-shore variations in morphodynamic processes of an open-coast mudflat in the Changjiang Delta, China: With an emphasis on storm impacts. Cont Shelf Res 2006; 26: 517–538.

[11] Kong LS, Gu FF, Wang W, et al. Statistics and analysis of typhoon-induced sudden siltation for Yangtze Estuary deepwater channel. Port Waterw Eng 2015; 503: 150–152.

[12] Chen AF, Emanuel KA, Chen DL, et al. Rising future tropical cyclone-induced extreme winds in the Mekong River Basin. Sci Bull 2020; 65 (5): 419–424.

[13] Li P, Yang SL, Milliman JD, et al. Spatial, temporal, and human-induced variations in suspended sediment concentration in the surface waters of the Yangtze Estuary and adjacent coastal areas. Estuar Coast 2012; 35: 1316–1327.

[14] Milliman JD, Shen HT, Yang ZS, et al. Transport and deposition of river sediment in the Changjiang Estuary and adjacent continental shelf. Cont Shelf Res 1985; 4: 37–45.

[15] Deng B, Wu H, Yang SL, et al. Longshore suspended sediment transport and its implications for submarine erosion off the Yangtze River Estuary. Estuarine, Coastl Shelf Sci 2017; 190: 1–10.

[16] Xiao SB, Li AC, Chen MT, et al. Recent 8 ka mud records of the east asian winter monsoon from the inner shelf of the East China Sea. J China Univ Geosci 2005; 30: 573–581.

[17] Xu K, Li A, Liu JP, et al. Provenance, structure, and formation of the mud wedge along inner continental shelf of the East China Sea: A synthesis of the Yangtze dispersal system. Mar Geol 2012; 291-294: 176–191.

[18] Liu JP, Li AC, Xu KH, et al. Sedimentary features of the Yangtze River-derived along-shelf clinoform deposit in the East China Sea. Cont Shelf Res 2006; 26: 2141–2156.

[19] Wang ZH, Saito Y, Zhan Q, et al. Three-dimensional evolution of the Yangtze River mouth, china during the holocene: Impacts of sea level, climate and human activity. Earth-Sci Rev 2018; 185: 938-955.

[20] Liao T, Cai TL, Liu YF, et al. Continental shoreline change in Zhejiang during the last one hundred years. J Mar Sci 2016; 34: 25-33.

[21] Du JL, Yang SL, Feng H. Recent human impacts on the morphological evolution of the Yangtze River Delta foreland: A review and new perspectives. Estuarine, Coastl Shelf Sci 2016; 181: 160-169.

[22] Puig P, Ogston AS, Mullenbach BL, et al. Storm-induced sediment gravity flows at the head of the Eel submarine canyon, northern California margin. J Geophys Res:Oceans 2004; 109(C3):C03019.

[23] Bhatia KT, Vecchi GA, Knutson T R, et al. Recent increases in tropical cyclone intensification rates. Nat Commun 2019; 10: 635.

[24] Singleton F. The Beaufort scale of winds - its relevance, and its use by sailors. Weather 2008; 63**:** 37–41.

[25] Whitehouse R et al. Dynamics of estuarine muds: A manual for practical applications. London: T. Telford, 2000.

[26] Woodroffe CD. Coasts: Form, process and evolution. Cambridge: Cambridge University Press, 2002.
[27] Fox WT, Davis RA. Computer model of wind, waves, and longshore currents during a coastal storm. J Int Assoc Math Geol 1979; 11: 143-164.
[28] Wu CS, Yang SL, Lei YP et al. Quantifying the anthropogenic and climatic impacts on water discharge and sediment load in the Pearl River (Zhujiang), China (1954–2009). J Hydrol 2012; 452–453: 190–204.
[29] Wu HL, Shen HT, Yan YX, et al. Preliminary study on sediment flux into the sea from Changjiang Estuary. Int J Sediment Res 2006; 75-81.
[30] Xie D, Pan C, Wu X, et al. The variations of sediment transport patterns in the outer Changjiang Estuary and Hangzhou Bay over the last 30 years. J Geophys Res 2017; 122: 2999–3020.
[31] Guo X, Fan D, Zheng S, et al. Revisited sediment budget with latest bathymetric data in the highly altered Yangtze (Changjiang) Estuary. Geomorphology 2021; 391: 107873.

4. Supplementary figures (shown below)

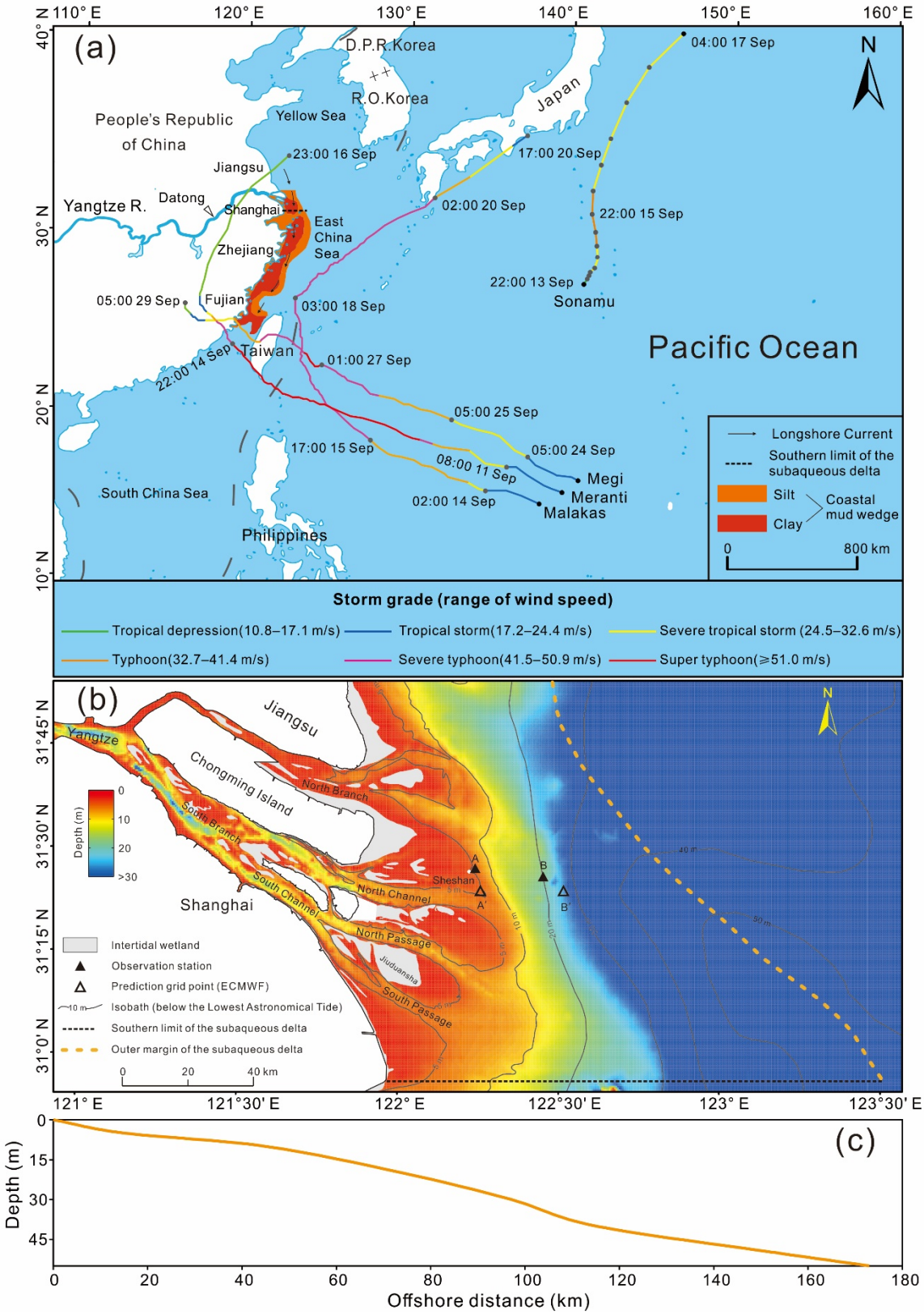

Fig. S1. Study area. (a) Locations of the Yangtze (Changjiang) River mouth, longshore current and coastal mud wedge, and the tracks of three typhoons (11–29 September, 2016). The longshore current and coastal mud wedge are modified after Xu et al. 2012 [17]. (b) Locations of the observation stations in the offshore subaqueous Yangtze Delta. ECMRWF: European Centre for Medium Range Weather Forecasts. (c) Cross-shore profile at the southern limit of the subaqueous Yangtze Delta. The location of the profile is marked by the black dashed line in Fig. 1b [Fig. S1a was drawn on the standard map downloaded from http://bzdt.ch.mnr.gov.cn/Map No: GS (2021) 5442].

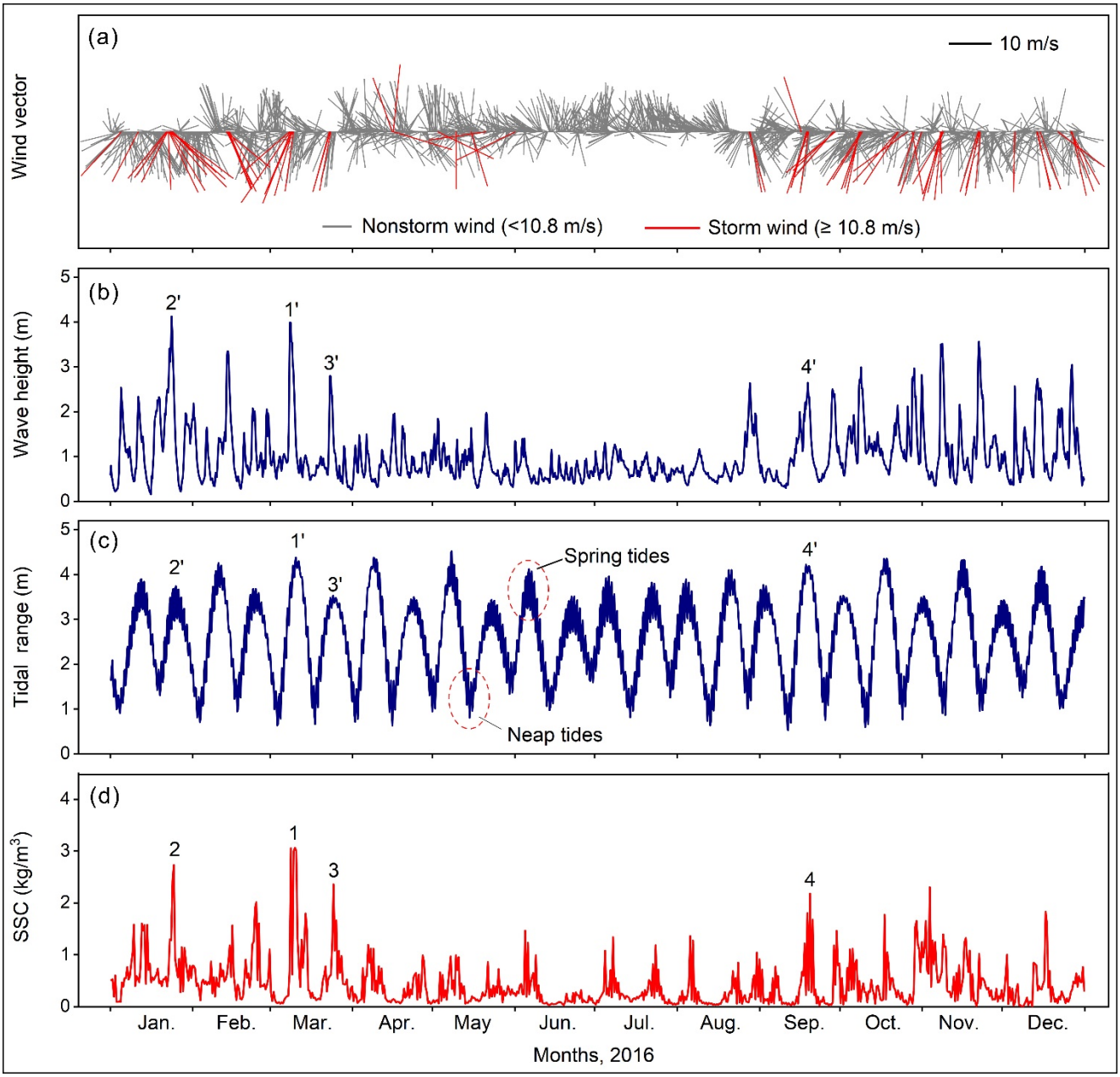

Fig. S2. Suspended sediment concentration (SSC) changes in response to wind, wave and tide at Station A in 2016. (a) Wind vector, (b) significant wave height, (c) tidal range and (d) surficial SSC. The temporal resolutions are (a) and (b) 6-hourly, (c) half a semidiurnal tidal cycle, and (d) twice daily. The numbers 1, 2, 3, and 4 in (d) indicate the four highest SSC events within the year; the numbers 1′, 2′, 3′ and 4′ in (b) and (c) indicate the corresponding peaks of wave height and tidal range.

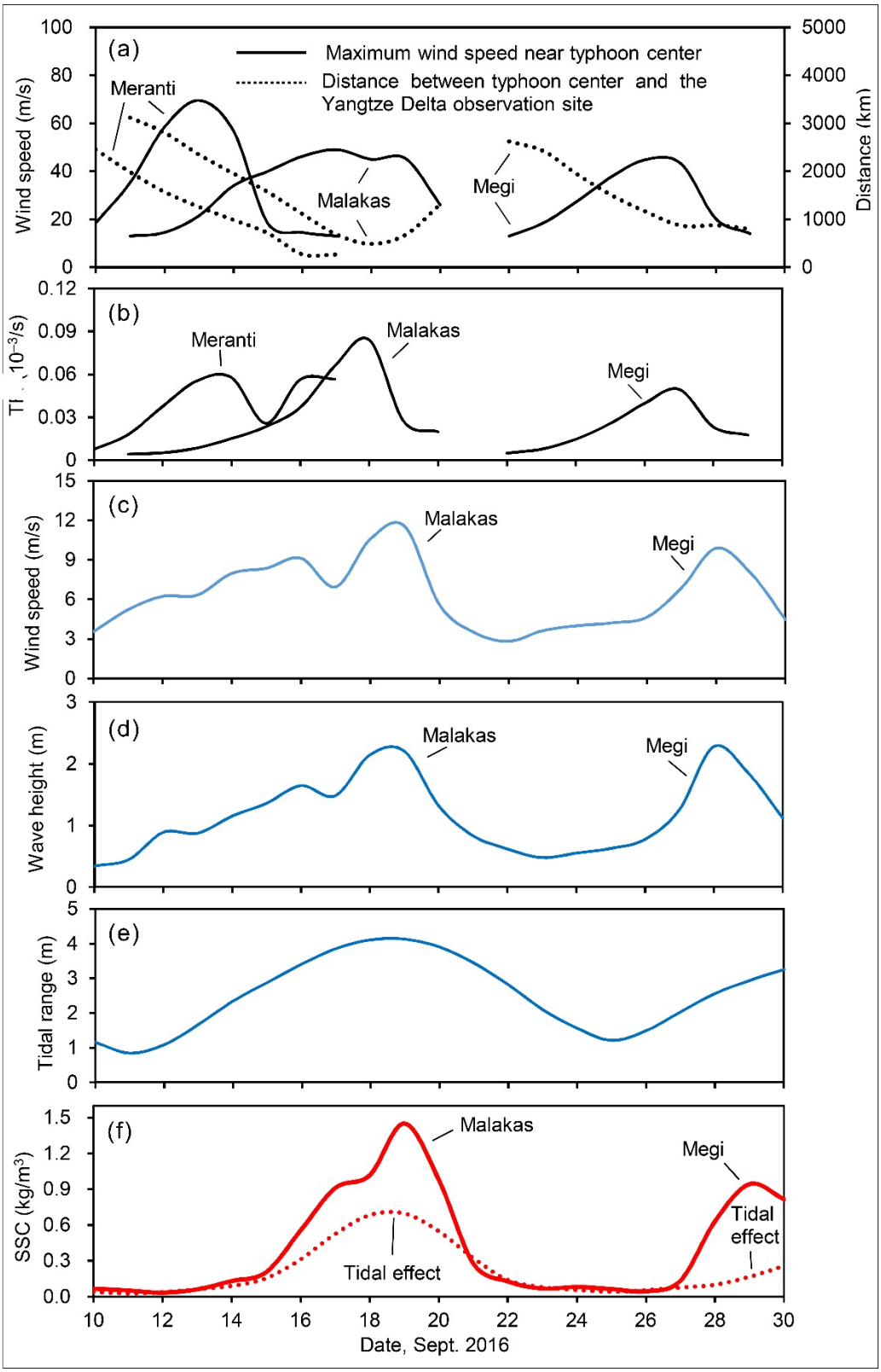

Fig. S3. Storm-induced sediment resuspension at Station A. (a) Maximum wind speed near the typhoon center and distance between the typhoon center and Station A. (b) Typhoon Force Index (TFI), defined as the ratio of the maximum wind speed near the typhoon center to the distance between the typhoon center and Station A (because the units of wind speed and distance are m/s and km, respectively, the unit of TFI is 10^{-3}/s). (c) Wind speed, (d) Significant wave height, (e) Tidal range, and (f) near-surface SSC at Station A. All data are day-averaged values. Meranti, Malakas and Megi are typhoon names. In (f), the dotted line represents tide-generated changes alone, and the difference between the solid and dotted lines reflects storm-generated changes.

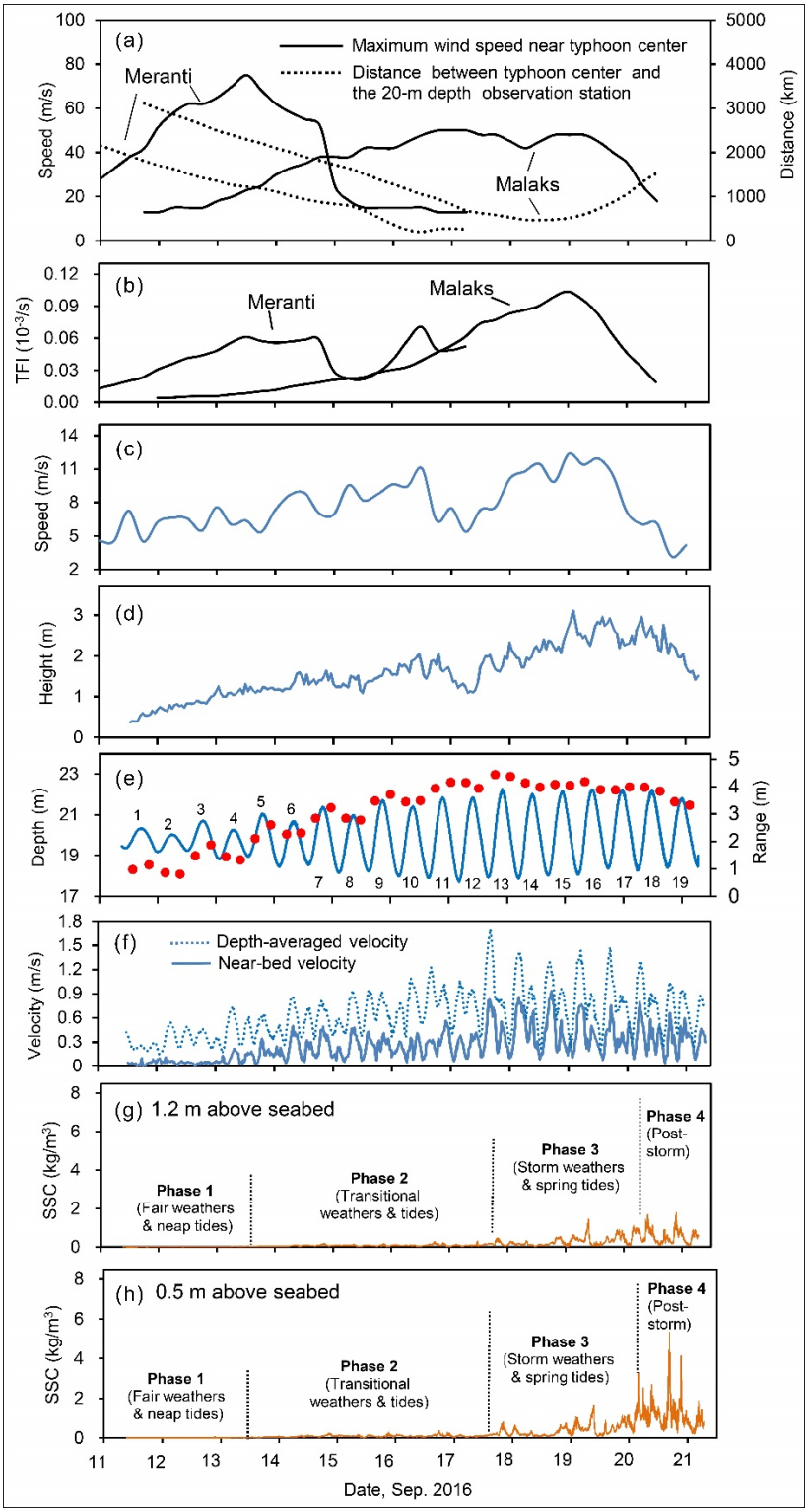

Fig. S4. Storm-induced sediment resuspension at Station B. (a) Maximum wind speed near the typhoon center and the distance between the typhoon center and Station B, (b) Typhoon Force Index (TFI), (c) Wind speed, (d) Significant wave height, (e) Water depth (line) and tidal range (dots) (numbers in the graph indicate tide sequence), (f) Near-bed (solid line) and depth-averaged (dotted line) current velocity, (g) SSC at 1.2 m above the seabed, and (h) SSC at 0.5 m above the seabed. The time resolutions are 6 h in (a)–(c), 1 h in (d), 1 min in water depth and half a tide-cycle in (e), 20 min in (f), and 1 min in (g) and (h). Note: during Phase 4, both the wave height and current velocity decreased as the typhoon disappeared and the spring tide transitioned to mean tide; however, the near-bed SSCs increased further, with SSC increased more rapidly at the lower layer (see Table S3 for phase-averaged SSC changes). This was attributed to downward decreasing settling velocity with downward increasing SSC, which leaded to enrichment of sediments in the near-bed layers. In fact, the near-surface SSC at Station A decreased rapidly in the post-Malakas phase (Fig. S3F, Table S3).

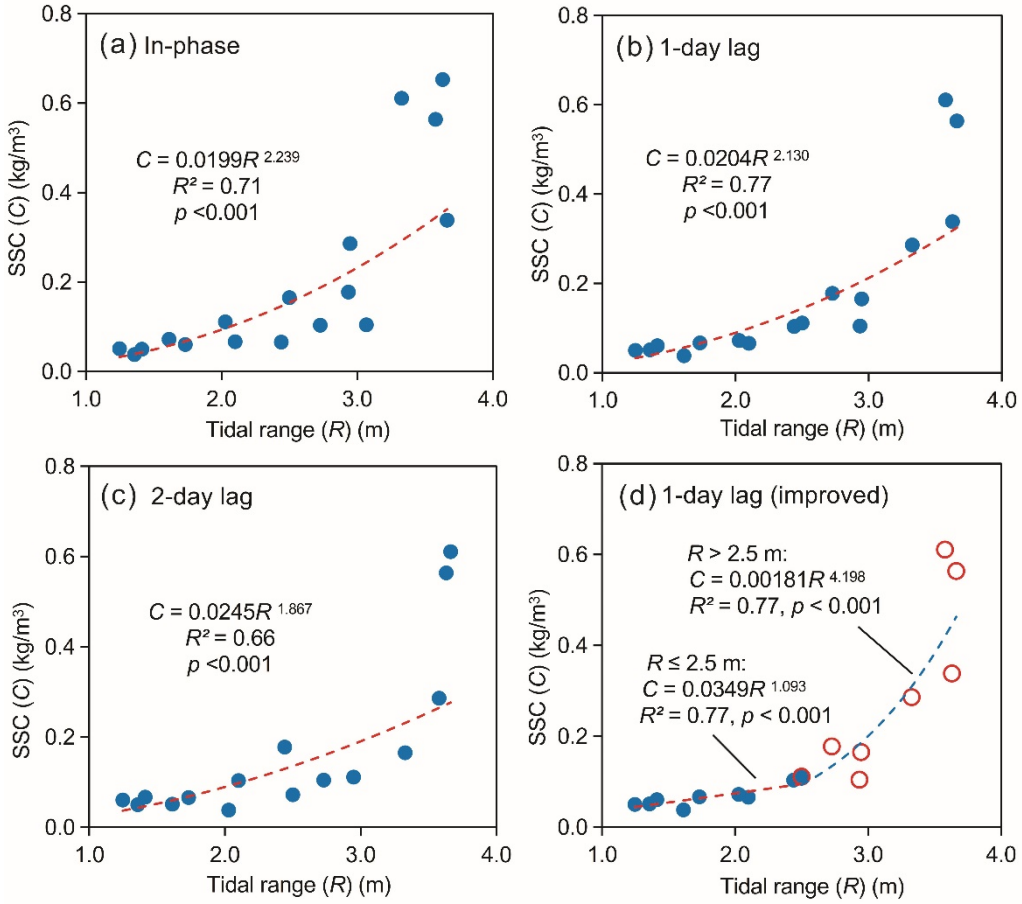

Fig. S5. Power-law correlations between the daily average tidal range (R) and surficial SSC (C) at Station A (the 7-m-depth station) under fair-weather conditions. (a) In-phase tidal range and SSC data (7–21 June 2016). (b) With a 1-day lag of SSC (7–21 June 2016) behind the tidal range (6–20 June 2016). (c) With a 2-day lag of SSC (7–21 June 2016) behind the tidal range (5–19 June 2016). (d) Improved 1-day lag relationships. As the coefficient of the 1-day lag relationship was significantly greater than the coefficients of the in-phase and 2-day lag correlations, and because the improved 1-day lag relationship overcomes underestimation of SSC for tidal ranges above 3.5 m, the improved 1-day lag relationship was used to predict the tide-induced SSC changes in this study.

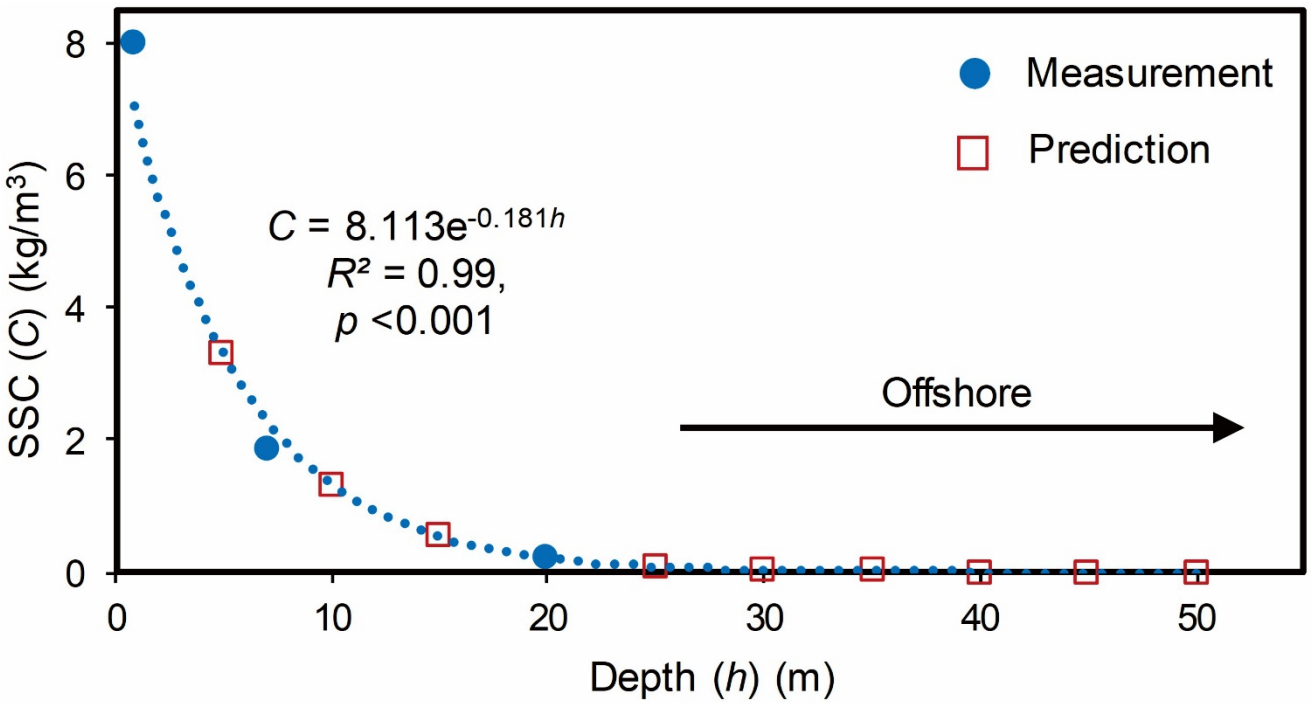

Fig. S6. Offshore trend in time-depth-averaged SSC against time-averaged water depth (below mean sea level) during Typhoon Malakas. The dotted line and equation represent the correlation trend between the measured SSC and mean water depth. The squares indicate SSC predictions at given water depths based on the trend equation. The measurement of SSC at water depth 0.5 m was estimated from data by Yang et al., 2019 [8].

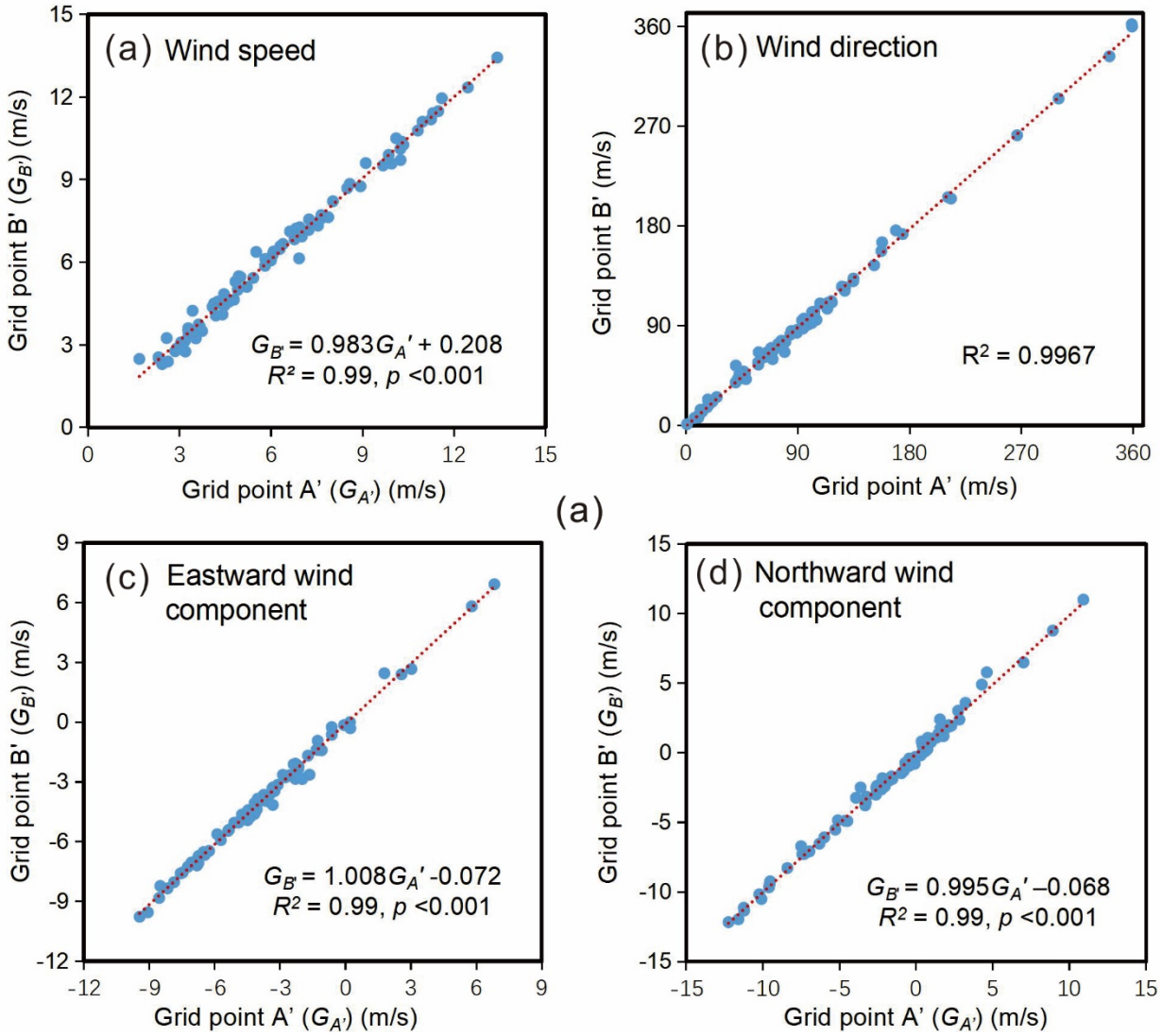

Fig. S7. Scatter diagrams between the wind parameters at Station A′ and those at Station B′. The data were derived from the ECMWF predictions (10–30 September 2016). The dot in the upper right corner in panel B represents a wind direction of 359° at Station A′ and a wind direction of 2° (plotted as 362°) at Station B′. The locations of Stations A′ and B′ are shown in Fig. S1b.

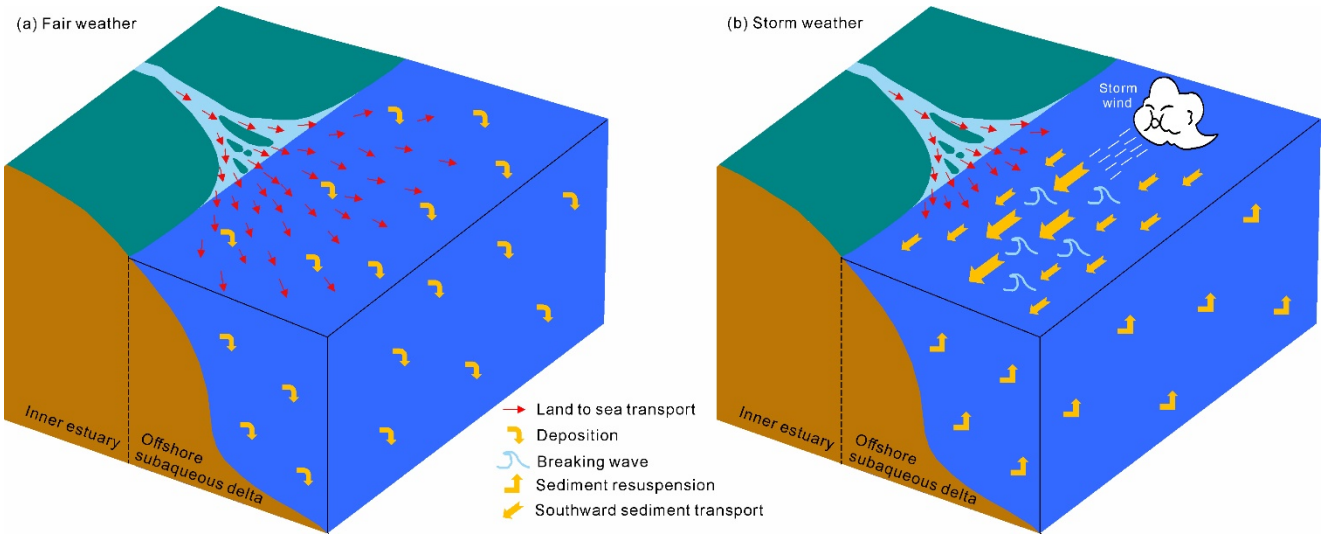

Fig. S8. A simplified conceptual model for the fate of Yangtze-derived sediments in (a) fair weather and (b) storm weather conditions. This model excludes the effects of tides and monsoon nonstorm winds on sediment transport. Although tides cause frequent alternation of deposition and resuspension, tide-induced net longshore sediment transport is negligible. The effect of the winter monsoon nonstorm winds is thought to be mostly neutralized by the effect of the summer monsoon nonstorm winds, and the monsoon-induced net southward sediment transport is minor in comparison with the storm-induced net southward sediment transport.

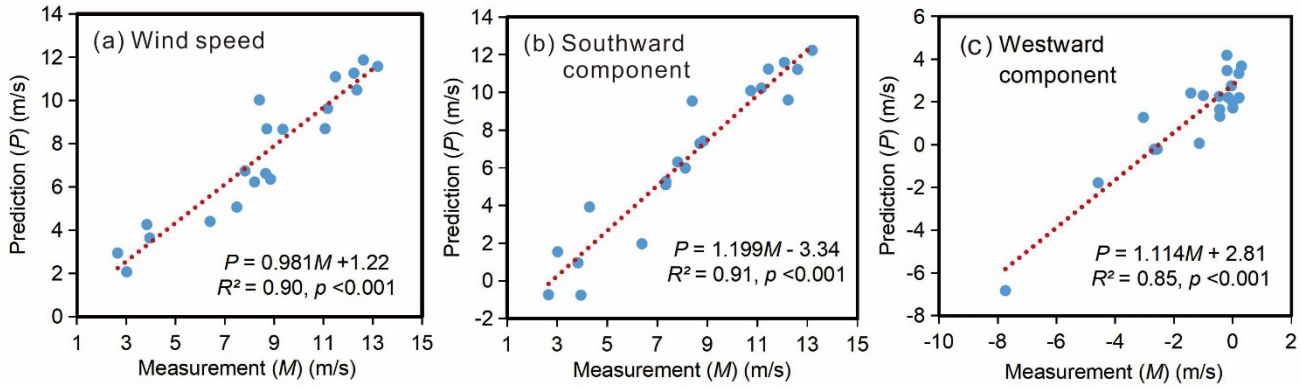

Fig. S9. Linear correlations between ECMWF-predicted wind parameters at Station A′ and measured wind parameters at Station A.

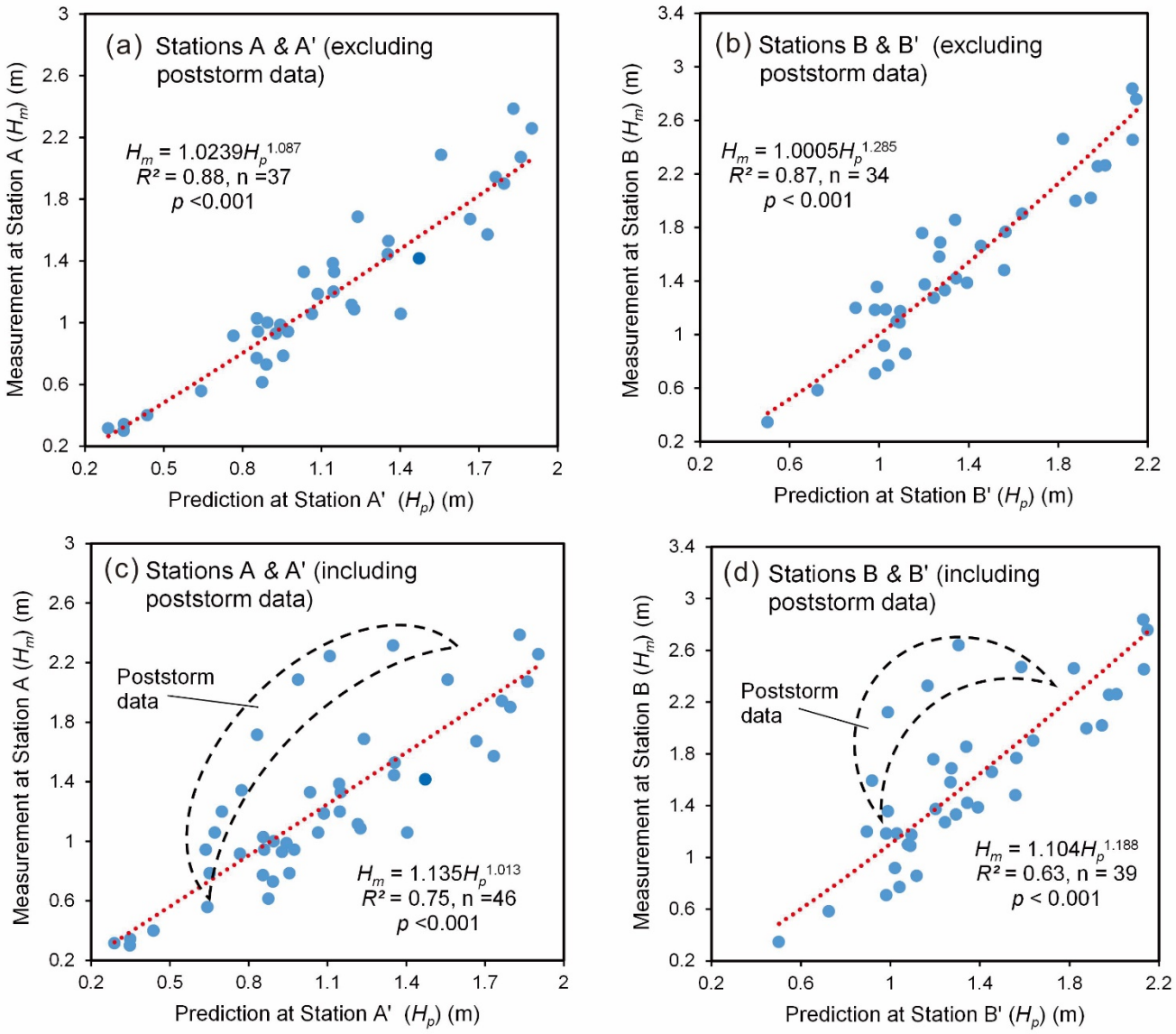

Fig. S10. Power-law correlations between the significant wave height measured in this study (H_m) and the significant wave height predicted by ECMWF (H_p). Both (a) and (b) represent a continuous period covering first a fair-weather stage and then a storm stage (a: 18:00 Sep 10–0:00 Sep 20, 2016; b: 12:00 Sep 11–0:00 Sep 20, 2016), whereas both (c) and (d) represent a continuous period covering first a fair-weather stage, then a storm stage, and afterwards a poststorm stage (c: 18:00 Sep 10–6:00 Sep 22, 2016; d: 12:00 Sep 11–6:00 Sep 21, 2016). The measured significant wave heights were shown in Figures 3 and 4. (c) and (d) suggest that the poststorm wave heights were notably higher than predicted, presumedly because of the propagation of wells from the open waters.

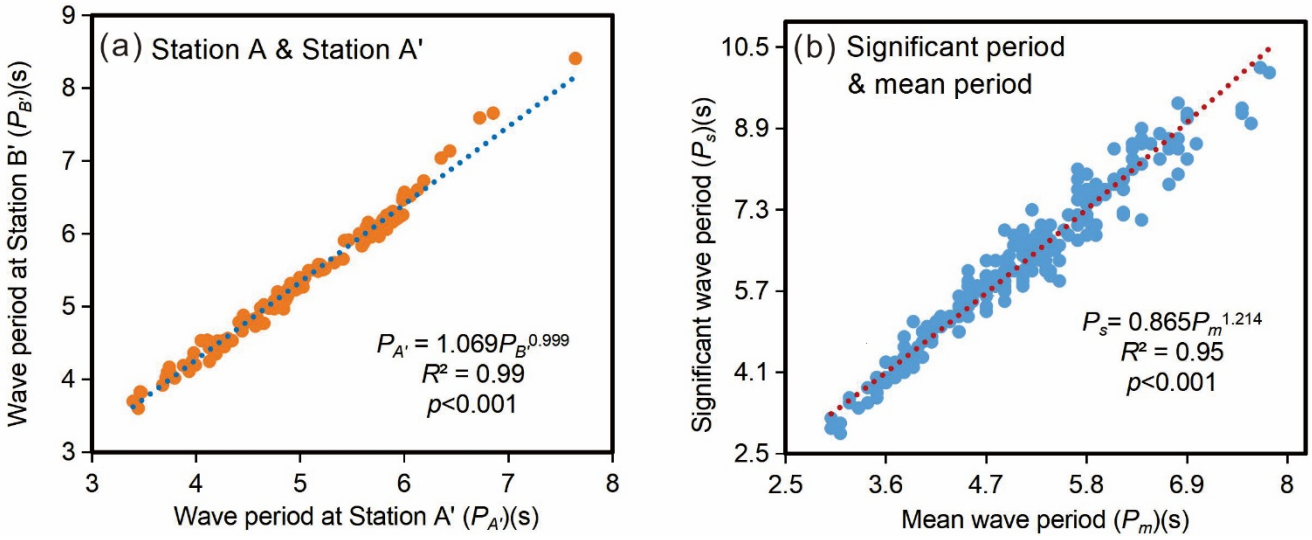

Fig. S11. Power-law correlations between the wave periods during the observation period. (a) Correlation between the mean wave periods at Stations A′ and B′; (b) Correlation between the significant and mean wave periods at Station A'.

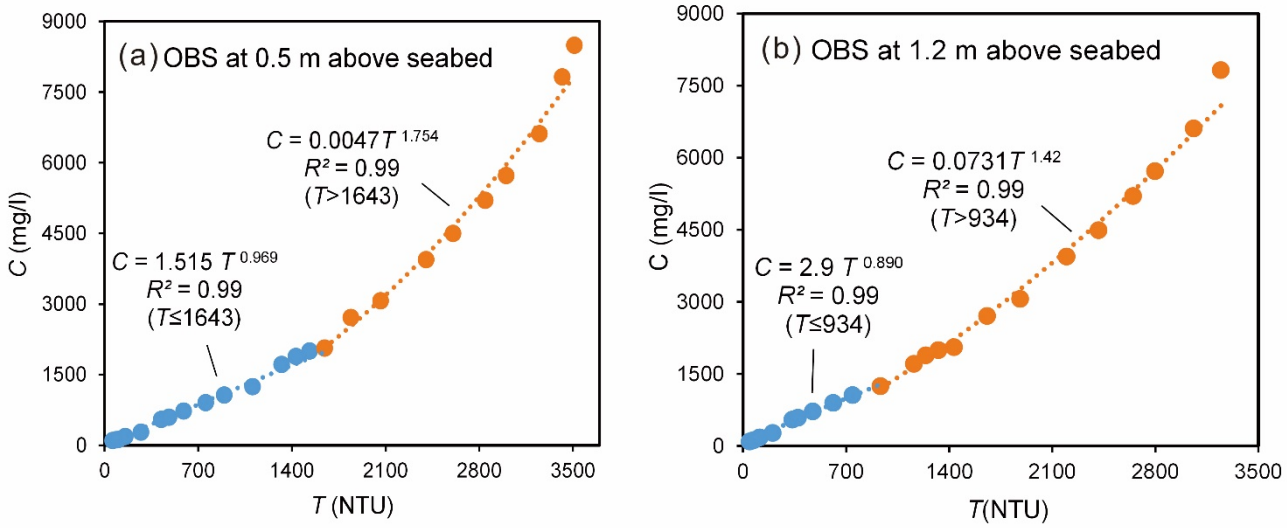

Fig. S12. Power-law correlations between the OBS turbidity (*T*) and SSC (*C*) based on a calibration using in situ sediment samples. NTU: nephelometric turbidity unit.

5. Supplementary tables (shown below)

Table S1. Cumulative southward, northward, westward and eastward components of storm and nonstorm winds at the offshore subaqueous Yangtze Delta in different years and seasons.

	Southward (longshore) component		Northward (longshore) component		Westward (onshore) component		Eastward (offshore) component	
	Storm wind (10^6 m/a)	Nonstorm wind (10^6 m/a)	Storm wind (10^6 m/a)	Nonstorm wind (10^6 m/a)	Storm wind (10^6 m/a)	Nonstorm wind (10^6 m/a)	Storm wind (10^6 m/a)	Nonstorm wind (10^6 m/a)
Annual data (1979–2018)								
1979	20.6	68.6	1.5	51.3	5.7	53.9	8.5	27.1
1980	16.0	81.8	3.0	44.7	0.8	59.4	7.1	28.7
1981	16.2	78.7	0.3	51.4	4.5	57.5	6.5	27.4
1982	13.0	76.4	1.4	45.4	6.2	60.6	6.5	24.8
1983	14.7	84.2	1.2	44.1	4.9	53.7	4.5	31.6
1984	16.9	81.5	1.6	42.3	3.8	71.2	4.1	19.1
1985	11.2	81.2	3.5	50.7	5.4	67.1	3.2	28.3
1986	13.6	79.5	0.4	48.2	2.8	54.8	5.4	26.6
1987	20.2	71.8	2.9	52.8	3.7	56.1	5.4	26.0
1988	14.0	90.4	1.1	37.7	2.6	60.7	4.3	26.5
1989	12.1	91.1	1.4	39.7	2.7	64.1	3.6	23.9
1990	17.2	69.4	4.0	55.7	5.2	61.6	5.0	24.2
1991	9.0	92.9	0.6	41.1	1.3	52.2	3.4	28.8
1992	12.3	80.8	3.1	46.3	7.4	53.3	4.5	28.2
1993	14.5	79.0	0.5	42.3	1.9	55.1	5.3	28.7
1994	11.6	77.7	4.3	53.2	6.9	58.4	3.6	24.1
1995	8.0	78.4	6.3	57.0	1.7	50.2	4.4	30.6
1996	14.6	72.6	2.9	49.8	5.2	59.8	4.5	26.3
1997	10.9	76.1	4.7	53.4	5.0	52.7	4.1	27.3
1998	13.6	72.8	2.8	49.4	5.1	58.0	3.2	27.8
1999	16.4	72.0	1.6	43.3	2.8	66.5	5.8	25.5
2000	18.4	72.6	3.9	50.3	8.0	69.7	3.4	22.2
2001	14.8	78.8	1.1	45.8	5.8	73.3	4.3	26.1
2002	14.5	71.6	4.5	46.0	5.9	59.3	4.7	30.3
2003	13.4	79.9	1.0	50.7	0.3	58.2	5.8	27.7
2004	17.1	72.5	2.6	56.0	5.5	62.9	6.0	22.1
2005	10.7	71.3	4.2	56.0	3.8	58.2	5.4	28.8
2006	10.5	74.4	4.8	48.8	6.8	60.2	2.3	25.9
2007	9.9	78.2	1.5	53.9	3.0	63.7	4.1	24.7
2008	10.9	70.6	2.9	49.0	3.4	59.7	3.5	27.1
2009	13.3	70.1	2.2	52.6	3.9	64.6	4.6	25.6
2010	19.6	65.1	1.3	59.1	3.7	60.6	5.1	27.4
2011	14.0	86.5	3.2	52.4	2.6	58.0	3.4	21.4
2012	16.1	79.5	2.4	48.9	6.3	72.1	5.5	25.1
2013	18.8	71.1	3.9	62.1	5.4	63.2	3.0	25.7
2014	15.8	73.1	2.2	46.9	5.3	66.5	4.6	25.2
2015	9.1	71.3	1.4	45.3	3.8	64.5	4.1	29.3
2016	**19.4**	**62.2**	**0.8**	**53.7**	**5.3**	**67.4**	**4.5**	**24.3**
2017	13.5	69.2	0.4	55.7	5.8	62.4	2.3	24.5
2018	15.2	69.4	3.4	58.1	6.8	73.6	4.2	19.2
Mean±std	14.3±3.2	76.1±6.8	2.4±1.5	49.8±5.6	4.4 ± 1.9	61.1 ± 6.0	4.6±1.3	26.1 ± 2.8
Seasonal data (2016)								
Spring	4.5	12.2	0.5	17.3	1.7	16.5	0.6	4.7
Summer	1.1	5.6	0.0	22.9	0.3	17.7	0.4	5.6
Autumn	7.2	20.2	0.2	5.8	2.5	22.4	0.0	4.2
Winter	6.6	24.2	0.1	7.7	0.8	10.8	3.5	9.8
Mean±std of seasonal data (1979–2018)								
Spring	1.9±1.1	16.2±2.4	0.7±0.7	16.2±2.8	0.6±0.4	15.8±2.1	0.5±0.3	5.7±1.2
Summer	0.7±0.8	6.5±2.0	1.4±1.2	22.6±3.7	1.6±1.2	16.2±3.1	0.3±0.4	5.5±1.4
Autumn	5.1±2.3	24.3±2.6	0.2±0.3	5.8±1.7	1.5±1.0	17.9±2.2	1.2±0.9	5.2±1.6
Winter	6.6±2.1	29.2±3.5	0.1±0.2	5.1±1.8	0.7±0.7	11.1±2.1	2.6±1.0	9.7±1.5

Note: This table is based on data at Station B′. *Cumulative wind component* means the product of wind speed and duration of the corresponding component. Storm wind: Wind speed ≥ 10.8 m/s. Nonstorm wind: Wind speed < 10.8 m/s.

Table S2. Storm wind frequency during different years and different seasons in the period 1979–2018 (%).

	Annual	Winter	Spring	Summer	Autumn
1979	7.3	7.8	2.1	5.7	13.7
1980	5.7	11.3	6.8	0.3	4.7
1981	5.3	6.9	0.8	1.4	12.1
1982	5.5	7.8	4.3	5.7	4.7
1983	5.2	6.7	3.8	2.7	7.4
1984	5.6	13.5	1.6	4.3	3.0
1985	4.9	8.3	1.9	5.2	4.1
1986	4.4	8.1	1.1	3.3	5.2
1987	6.8	12.8	4.9	2.7	6.9
1988	4.6	6.6	3.8	1.4	6.9
1989	4.2	3.6	2.7	2.4	8.0
1990	6.6	10.3	1.9	3.3	11.3
1991	3.0	6.4	1.6	0.3	3.5
1992	5.5	4.7	3.3	4.1	10.2
1993	4.7	12.8	0.8	1.4	3.8
1994	5.5	6.4	2.4	8.4	4.9
1995	4.5	3.9	3.8	5.5	4.7
1996	5.7	9.1	2.7	3.3	8.0
1997	4.9	8.1	0.5	6.3	4.9
1998	5.0	10.0	3.0	1.4	5.5
1999	5.7	7.8	4.9	1.4	8.8
2000	6.7	8.0	2.7	5.4	11.0
2001	5.3	13.3	1.9	1.1	4.9
2002	6.2	8.1	3.3	6.5	6.9
2003	4.4	8.9	4.3	0.0	4.7
2004	6.4	9.9	3.8	5.2	6.6
2005	4.7	8.3	3.3	3.8	3.6
2006	5.1	5.0	6.0	3.3	6.0
2007	3.6	5.8	3.8	1.1	3.8
2008	4.5	8.2	1.4	4.1	4.4
2009	4.9	9.2	3.0	1.1	6.3
2010	6.3	13.9	5.2	0.3	6.6
2011	5.1	6.9	4.9	3.0	5.5
2012	6.3	10.2	3.0	5.4	6.5
2013	6.8	6.7	7.1	4.3	9.3
2014	5.7	10.3	2.4	4.1	6.0
2015	3.9	5.0	3.3	3.5	3.8
2016	**6.1**	**9.6**	**5.2**	**1.4**	**8.5**
2017	4.5	6.1	0.3	0.3	11.5
2018	6.1	11.1	4.6	4.9	3.8
Mean±std	5.3±0.9	8.4±2.6	3.2±1.7	3.2±2.1	6.6±2.7

Note: Storm wind frequency is defined as the ratio of storm wind (wind speed $\geqslant$ 10.8 m/s) duration to the entire time period of the corresponding year or season. Winter: December to February. Spring: March to May. Summer: June to August. Autumn: September to November.

Table S3. Time-averaged values (±standard deviation) of wind speed, wave parameters, tidal range, current velocity, near-bed SSC at observation Stations A and B, and riverine water discharge and SSC at Datong Station (see Fig. S1 for the locations of these station), in a prestorm period (Phases 1–2), a storm event (Typhoon Malakas, Phases 3), and a poststorm period (Phases 4) (11–21 September 2016).

Periods	S_w (m/s)	H_s (m)	P_m (s)	L_m (m)	R_t (m)	V_a (cm/s)	V_n (cm/s)	Q (10^3 m^3/s)	C_r (mg/l)	$C_{0.5\,m}$ (mg/l)	$C_{1.2\,m}$ (mg/l)	C_s (mg/l)
Station A												
Phase 1	5.8±1.0	0.7±0.2	4.0±0.7	25±7	1.2±0.5	ND	ND	28.5±0.9	102±4	ND	ND	48±10
Phase 2	7.7±1.3	1.2±0.2	4.8±0.5	34±6	2.8±0.7	ND	ND	26.3±1.0	102±5	ND	ND	350±330
Phase 3	10.1±1.3	1.9±0.4	5.5±0.6	39±6	4.1±0.1	ND	ND	24.4±0.8	98±9	ND	ND	1100±260
Phase 4	5.3±1.2	1.8±0.4	6.7±0.6	52±7	3.8±0.2	ND	ND	23.2±0.7	87±2	ND	ND	580±510
Station B												
Phase 1	5.9±1.1	0.8±0.2	4.4±0.7	31±10	1.2±0.4	34±13	6±4	28.5±0.9	102±4	12±7	11±7	ND
Phase 2	7.9±1.5	1.5±0.3	5.4±0.7	46±12	3.2±0.7	67±23	25±14	26.3±1.0	102±5	91±43	76±36	ND
Phase 3	10.4±1.4	2.3±0.4	5.9±0.9	55±17	4.1±0.2	83±33	40±22	24.4±0.8	98±9	462±391	309±247	ND
Phase 4	5.5±1.3	2.1±0.4	7.3±0.7	76±10	3.7±0.4	72±24	33±15	23.2±0.7	87±2	1122±665[1]	541±324[1]	ND

Note: A storm event is defined as a period when the storm winds (≥ 10.8 m/s) last for at least 6 hours and the time-averaged wind speed is ≥ 10 m/s. S_w: Wind speed. H_s: Significant wave height. P_m: Mean wave period. L_m: Mean wavelength. R_t: Tidal range. V_a: Depth-averaged current velocity. V_n: Near-bed (1.2 m above seabed) current velocity. Q: Water discharge of the Yangtze River at the most seaward station (Datong). C_r: SSC of the Yangtze River at the most seaward station (Datong). $C_{0.5\,m}$: SSC at 0.5 m above the seabed. $C_{1.2\,m}$: SSC at 1.2 m above the seabed. C_s: SSC at the water surface. ND: No data. Phase 1: Tides 1–4 (10:37 Sep 11–13:15 Sep 13). Phase 2: Tides 5–12 (13:15 Sep 13–16:14 Sep 17). Phase 3: Tides 13–17 (16:14 Sep 17–5:37 Sep 20). Phase 4: Tides 18–19 (5:37 Sep 20–6:29 Sep 21). The calculation of wavelength is based on the equations for Airy wave theory: $L_{deep} = gT^2/2\pi$ ($h/L > 0.25$), $L_{transitional} = (gT^2/2\pi)$ (tanh[$2\pi h/L$]) ($0.25 > h/L > 0.05$), $L_{shallow} = T\,(gh)^{0.5}$ ($h/L < 0.05$), where L is the wavelength, $g = 9.81$ m/s^2, T is the wave period, $\pi = 3.1316$, and h is the water depth [26]. [1]The SSC increase from Phase 3 to Phase 4 is explained in the caption of Fig. S4. The large standard deviations in columns 7–8 and 11–13 reflect intratidal and intertidal variabilities in flow velocity and SSC.

Table S4.1. Residual current velocities (cm/s) of individual tidal cycles in different water layers at Station B (the 20-m-depth station) compared with the residual wind speed (cm/s) in the same time period.

Height (m)[a]	Tide 1	Tide 2	Tide 3	Tide 4	Tide 5	Tide 6	Tide 7	Tide 8	Tide 9	Tide 10	Tide 11	Tide 12	Tide 13	Tide 14	Tide 15	Tide 16	Tide 17	Tide 18	Tide 19
17.5	8	20	16	21	29	27	38	20	28	45	18	45	72	39	44	42	29	20	15
17.0	9	26	12	26	24	31	34	22	26	42	17	53	71	38	43	42	28	20	11
16.5	11	28	6	31	22	34	30	25	23	38	21	61	70	36	42	40	27	21	10
16.0	12	29	2	35	19	36	27	25	19	34	18	57	70	36	41	41	27	20	10
15.5	12	30	7	36	17	36	23	25	16	29	16	49	69	35	41	40	28	21	9
15.0	11	27	12	36	17	37	18	25	10	25	12	42	67	34	41	40	27	20	10
14.5	10	24	16	36	16	36	15	24	5	21	11	36	67	34	40	40	27	19	10
14.0	8	22	17	35	16	35	13	22	0	18	10	31	66	33	40	39	26	19	10
13.5	8	22	15	33	15	32	13	21	3	15	10	27	64	32	40	39	26	19	8
13.0	9	20	13	32	14	29	13	18	6	12	9	24	62	31	40	39	26	18	9
12.5	7	19	12	29	13	26	14	18	9	11	10	22	62	31	39	38	25	17	9
12.0	6	18	11	29	13	22	14	17	9	9	10	19	60	31	38	38	25	17	9
11.5	6	17	10	28	13	18	14	17	10	5	10	18	58	30	37	37	24	17	8
11.0	5	16	9	26	12	16	14	16	11	3	11	17	56	29	36	37	24	16	8
10.5	4	16	9	24	10	14	13	16	11	1	12	17	55	29	35	35	23	15	7
10.0	4	17	8	21	11	12	12	14	11	4	12	15	53	28	35	35	23	15	7
9.5	3	18	9	19	11	11	12	13	11	6	13	13	52	28	33	35	22	14	7
9.0	3	17	8	18	11	10	11	12	10	9	14	13	50	28	33	33	21	13	8
8.5	3	15	8	15	11	7	12	11	9	10	16	11	49	28	32	32	21	13	7
8.0	3	13	9	13	11	6	12	10	9	11	17	9	47	26	31	31	21	12	7
7.5	2	11	10	12	11	5	11	9	9	14	18	8	46	26	30	30	20	11	7
7.0	2	10	10	11	11	5	10	9	9	16	18	7	45	26	29	29	19	10	7
6.5	4	10	10	10	11	5	9	7	9	15	18	6	42	25	27	27	18	10	7
6.0)	5	9	11	10	11	6	9	8	11	15	18	6	40	26	26	27	18	10	7
5.5	6	9	10	9	10	5	8	9	10	15	19	5	39	25	24	24	17	9	7
5.0	7	9	10	11	9	5	7	8	9	15	19	5	38	25	24	23	16	7	6
4.5	7	8	10	10	10	5	8	9	9	14	19	6	35	24	22	22	15	8	7
4.0	6	8	10	9	10	5	8	9	7	14	19	6	33	24	21	21	14	8	7
3.5	6	8	9	10	9	5	8	8	6	11	17	6	32	23	20	20	14	7	7
3.0	6	8	9	9	9	5	7	9	8	12	19	7	30	23	19	18	12	6	6
2.5	5	7	8	9	9	5	7	6	6	10	21	5	27	22	17	17	11	7	6
2.0	4	7	4	7	7	4	13	20	11	13	32	5	25	22	16	15	10	8	7
1.5	2	4	1	2	4	6	9	7	1	5	9	7	23	21	15	14	5	2	7
Entire column[b]	6	15	9	18	12	15	13	14	10	15	14	19	48	28	30	30	19	12	8
Wind speed	5.4	6.3	6.4	5.9	6.2	6.3	8.2	8.1	8.7	9.3	4.8	6.1	8.9	10.9	11.2	11.3	8.1	6.4	4.5

[a]Each height represents the midpoint of a 0.5-m layer above the seabed. [b]Overall residual current velocity of the entire water column. Each velocity in each layer and each tide is a tidal residual rather than a time-averaged value. Therefore, the intratidal changes in flow velocity should not be included in uncertainty range. The uncertainty range of the residual current velocity is ±0.25%, which reflects the measurement error (see Section 2.12 in the Supplementary Materials online). These uncertainty ranges are not listed in the table because of space limitations. The standard deviation which reflects intratidal (cyclic) changes in flow velocity is not included in the uncertainty range.

Table S4.2. Residual current directions (°) of individual tidal cycles in different water layers at Station B (the 20-m-depth station) compared with the residual wind direction (°) in the same time period.

Height (m)[a]	Tide 1	Tide 2	Tide 3	Tide 4	Tide 5	Tide 6	Tide 7	Tide 8	Tide 9	Tide 10	Tide 11	Tide 12	Tide 13	Tide 14	Tide 15	Tide 16	Tide 17	Tide 18	Tide 19
17.5	176	25	9	356	1	18	11	25	343	5	78	183	192	207	184	181	193	197	244
17.0	163	31	9	0	359	23	11	47	353	11	106	175	188	204	183	179	192	188	233
16.5	149	36	357	2	350	18	7	46	359	15	120	170	187	203	182	179	190	185	220
16.0	144	38	251	4	341	17	6	44	2	17	133	168	186	202	183	178	189	181	221
15.5	139	34	208	5	145	17	179	43	360	19	147	167	185	202	183	178	190	183	224
15.0	138	31	200	6	313	16	351	39	354	22	159	167	184	200	182	178	190	183	221
14.5	132	27	207	7	302	16	333	33	344	23	173	169	183	200	181	178	189	184	226
14.0	131	23	209	6	291	11	315	28	317	28	190	171	181	200	181	177	189	183	223
13.5	141	23	217	4	285	2	305	19	161	32	200	172	180	198	181	177	189	184	229
13.0	144	17	226	1	275	354	304	11	154	31	217	172	178	198	181	177	188	184	226
12.5	142	15.7	232	355	264	345	309	1.36	156	31.2	220	167	176	197	181	175	189	186	230
12.0	144	10	242	171	252	338	310	353	161	32	221	166	176	195	181	175	189	187	225
11.5	144	5	246	167	255	329	313	344	165	38	219	166	175	194	182	175	189	189	231
11.0	151	356	251	344	258	318	316	336	170	19.2	226	165	172	194	181	174	190	190	233
10.5	160	348	258	340	272	307	316	330	176	309	232	165	172	193	182	174	189	191	234
10.0	163	344	265	333	297	298	314	321	181	263	231	165	170	190	180	174	189	191	234
9.5	176	338	281	327	312	290	312	314	184	254	235	164	168	190	180	174	190	194	237
9.0	182	334	297	326	332	285	321	307	191	260	241	167	166	188	180	173	188	194	240
8.5	182	331	317	321	347	277	327	300	206	258	249	165	166	187	179	173	188	197	248
8.0	166	320	333	314	359	267	334	297	213	259	252	163	164	184	178	171	187	197	247
7.5	137	309	346	312	9	253	337	294	224	263	257	156	162	182	178	174	187	201	255
7.0	74	297	357	309	19	251	159	114	230	263	260	149	161	182	178	175	187	200	253
6.5	61	291	8	303	23	263	350	296	240	263	261	135	159	179	176	173	188	203	257
6.0	64	282	18	288	27	253	336	290	244	266	264	127	158	179	174	170	186	205	263
5.5	69	277	33	285	32	259	342	284	240	267	267	125	157	180	174	182	190	211	266
5.0	72	277	43	286	38	263	347	284	245	270	273	110	156	177	172	183	188	208	269
4.5	69	286	47	290	35	281	332	287	246	276	273	106	154	177	172	179	186	208	98
4.0	59	289	44	295	32	283	333	290	243	277	274	101	153	178	170	182	183	212	286
3.5	56	287	42	293	35	293	334	294	249	277	280	102	152	175	169	183	181	216	286
3.0	53	292	45	292	35	285	333	297	252	280	278	99	151	175	165	187	183	228	293
2.5	53	289	397	302	34	294	339	314	70	284	280	91	153	175	163	208	185	230	290
2.0	116	244	100	300	41	328	312	290	263	283	282	104	150	176	163	186	201	246	290
1.5	195	222	179	297	35	318	346	324	315	286	308	120	158	176	152	169	160	231	308
Mean[b]	130	1	308	345	337	352	341	353	276	343	240	167	173	191	179	177	190	193	245
Wind speed	68	47	59	66	64	71	82	99	128	170	230	342	19	18	11	4	8	17	60

[a]Each height represents the midpoint of a 0.5-m water layer above seabed. [b]Overall residual current velocity of the entire water column.

Table S5. Residual suspended sediment transport and influencing factors at Station B during different tidal cycles and phases.

Periods	S_w (m/s)	D_w (°)	V_s (cm/s)	D_s (°)	V_a (cm/s)	D_a (°)	H_s (m)	R_t (m)	C_a (mg/l)	F_s (g/s)
Phase 1: Fair weather and neap tides (Wave height, flow velocity, SSC and rate of sediment transport rate were low)										
Tide 1 (10:37–23:56 Sep 11)	4.7	68	8±0.02	181	6±0.02	130	0.33	0.96	4±0.3	4±0.3
Tide 2 (23:56 Sep 11–12:21 Sep 12)	5.6	47	20±0.05	7	15±0.04	1	0.60	0.85	5±0.4	16±1.3
Tide 3 (12:21 Sep 12–1:21 Sep 13)	5.6	59	16±0.04	6	9±0.02	308	0.76	1.47	7±0.5	13±1.0
Tide 4 (1:21–13:15 Sep 13)	5.2	66	21±0.05	343	18±0.05	345	0.94	1.44	13±0.8	45±2.9
Phase 1	**5.3**	**59**	**11**±0.02	**358**	**7**±0.03	**354**	**0.66**	**1.18**	**7**±0.5	**9**±0.7
Phase 2: Transitional weather and tides (Wave height, flow velocity, SSC and sediment transport rate increased)										
Tide 5 (13:15 Sep 13–2:10 Sep 14)	6.2	64	29±0.07	1	12±0.03	337	1.05	2.36	25±1.4	63±3.7
Tide 6 (2:10–14:08 Sep 14)	6.3	71	27±0.07	358	15±0.04	352	1.23	2.28	41±2.2	119±6.7
Tide 7 (14:08 Sep 14–2:42 Sep 15)	8.2	82	38±0.10	8	13±0.03	341	1.42	3.04	64±3.4	168±9.2
Tide 8 (2:42–14:48 Sep 15)	8.1	99	20±0.05	2	14±0.05	353	1.32	2.81	55±2.9	150±8.3
Tide 9 (14:48 Sep 15–3:29 Sep 16)	8.7	128	28±0.07	338	10±0.03	276	1.80	3.59	58±3.1	119±6.7
Tide 10 (3:29–15:38 Sep 16)	9.3	170	45±0.11	1	15±0.04	343	2.51	3.47	49±2.7	143±8.2
Tide 11 (15:38 Sep 16–4:15 Sep 17)	4.8	230	18±0.05	79	14±0.04	240	1.60	4.04	80±4.2	228±13
Tide 12 (4:15–16:14 Sep 17)	6.1	342	45±0.11	166	19±0.05	167	2.50	4.04	59±3.1	217±12
Phase 2	**4.6**	**104**	**18**±0.04	**14**	**5**±0.01	**328**	**1.68**	**3.20**	**54**±2.9	**54**±3.0
Phase 3: Stormy weather and spring tides (Wave height, flow velocity, SSC and rate of sediment transport were highest)										
Tide 13 (16:14 Sep 17–4:48 Sep 18)	8.9	19	72±0.18	193	48±0.12	173	3.14	4.32	153±9.5	1490±97
Tide 14 (4:48–16:53 Sep 18)	10.9	18	39±0.10	208	28±0.07	191	3.41	4.12	87±4.6	475±27
Tide 15 (16:53 Sep 18–5:08 Sep 19)	11.2	11	44±0.11	187	30±0.08	179	4.34	4.12	232±14	1370±86
Tide 16 (5:08–17:32 Sep 19)	11.3	4	42±0.11	184	30±0.08	177	5.00	4.19	256±15	1540±94
Tide 17 (17:32 Sep 19–5:37 Sep 20)	8.1	8	29±0.07	198	19±0.05	190	4.26	3.86	422±23	1560±89
Phase 3	**10.1**	**12**	**45**±0.11	**193**	**32**±0.08	**180**	**4.03**	**4.12**	**230**±14	**1480**±93
Phase 4: Poststorm fair weather and spring–mean tides (Wave height, flow velocity, SSC and rate of sediment transport decreased)										
Tide 18 (5:37–18:13 Sep 20)	6.4	17	20±0.05	203	12±0.03	193	2.99	3.92	216±13	526±33
Tide 19 (18:13 Sep 20–6:29 Sep 21)	4.5	60	15±0.04	259	8±0.02	245	1.94	3.38	190±12	300±20
Phase 4	**4.6**	**33**	**17**±0.05	**227**	**10**±0.03	**211**	**2.47**	**3.65**	**203**±12	**410**±26

S_w: Time-averaged residual wind speed. D_w: Time-averaged residual wind direction. V_s: Time-averaged residual flow velocity at the water surface. D_s: Time-averaged residual flow direction at the water surface. V_a: Depth-time-averaged residual flow velocity. D_a: Depth-time-averaged residual flow and sediment transport direction. H_s: Significant wave height. R_t: Tidal range. C_a: Depth-averaged SSC. F_s: Rate of time-averaged residual sediment transport per meter width of the water column (mean depth 20 m). The uncertainty ranges of V_s and V_a are ±0.25%, which show the error of flow measurement (see Section 2.12). As shown in the notes of Table S4.1., the tide-induced cyclic changes in flow velocity are not listed in this table, because the velocity is residual. The uncertainty range of C_a reflects the combined impact of the measured error in turbidity (see Section 2.12) and the deviations between SSC and turbidity and relative depth (see Fig. S12). The uncertainty range of F_s reflects the combined impact of the measurement errors of flow velocity and turbidity, and the deviations between SSC and turbidity and relative depth (see Fig. S12). In other words, the intratidal and intertidal changes in flow velocity and SSC are not included in the uncertainty range of the sediment transport rate in this table.

Table S6. Amount of sediment transported southward from the Yangtze Delta during the Typhoon Malaks event. The total amount represents the sum of sediment transport through the cross-shore section at the south limit of the offshore subaqueous Yangtze Delta. The duration of the Typhoon Malaks event was 61 hours.

Water depth of subsection (m)	h (m)	C_a (mg/l)	V_a (cm/s)	T (s)	L (m)	T_s (kt)
0–1	0.5	7460±445	32±0.08	224,640	1,358	364±24
1–2	1.5	6220±373	32±0.08	224,640	2,383	1598±105
2–3	2.5	5160±311	32±0.08	224,640	2,505	2323±151
3–4	3.5	4240±255	32±0.08	224,640	2,962	3160±205
4–5	4.5	3450±207	32±0.08	224,640	3,463	3864±251
5–6	5.5	2760±167	32±0.08	224,640	4,227	4613±301
6–7	6.5	2170±131	32±0.08	224,640	6,925	7022±456
7–8	7.5	1750±106	32±0.08	224,640	6,227	5875±382
8–9	8.5	1480±90	32±0.08	224,640	6,808	6156±401
9–10	9.5	1270±77	32±0.08	224,640	4,831	4190±272
10–11	10.5	1090±65	32±0.08	224,640	4,257	3502±228
11–12	11.5	929±56	32±0.08	224,640	3,625	2784±181
12–13	12.5	795±49	32±0.08	224,640	3,174	2267±147
13–14	13.5	679±41	32±0.08	224,640	3,370	2220±144
14–15	14.5	582±35	32±0.08	224,640	2,674	1622±105
15–16	15.5	494±31	32±0.08	224,640	3,289	1810±118
16–17	16.5	414±25	32±0.08	224,640	2,398	1178±77
17–18	17.5	348±21	32±0.08	224,640	2,384	1044±68
18–19	18.5	294±18	32±0.08	224,640	2,553	998±65
19–20	19.5	250±15	32±0.08	224,640	2,713	951±62
20–21	20.5	211±13	32±0.08	224,640	2,603	809±53
21–22	21.5	174±10	32±0.08	224,640	2,774	746±48
22–23	22.5	144±8.5	32±0.08	224,640	2,386	556±36
23–24	23.5	118±7.1	32±0.08	224,640	2,193	437±28
24–25	24.5	97±5.8	32±0.08	224,640	2,275	390±25
25–26	25.5	80.8±4.8	32±0.08	224,640	2,430	360±23
26–27	26.5	67.4±4.1	32±0.08	224,640	2,486	319±21
27–28	27.5	56.3±3.4	32±0.08	224,640	2,019	225±15
28–29	28.5	47±2.8	32±0.08	224,640	2,217	213±14
29–30	29.5	39.2±2.4	32±0.08	224,640	2,114	176±11
30–31	30.5	32.7±2.0	32±0.08	224,640	1,987	142±9.2
31–32	31.5	27.3±1.6	32±0.08	224,640	1,510	93.3±6.1
32–33	32.5	22.8±1.5	32±0.08	224,640	1,614	86±5.6
33–34	33.5	19±1.2	32±0.08	224,640	1,759	80.5±5.2
34–35	34.5	15.9±1.1	32±0.08	224,640	1,564	61.7±4.1
35–36	35.5	13.2±0.8	32±0.08	224,640	1,338	45.1±2.9
36–37	36.5	11±0.7	32±0.08	224,640	1,619	46.7±3.1
37–38	37.5	9.2±0.6	32±0.08	224,640	1,912	47.4±3.1
38–39	38.5	7.7±0.5	32±0.08	224,640	2,187	46.5±3.1
39–40	39.5	6.4±0.4	32±0.08	224,640	2,302	42±2.7
40–41	40.5	5.4±0.3	32±0.08	224,640	2,742	42.7±2.8
41–42	41.5	4.5±0.3	32±0.08	224,640	2,994	39.9±2.7
42–43	42.5	3.7±0.2	32±0.08	224,640	3,481	39.6±2.6
43–44	43.5	3.1±0.2	32±0.08	224,640	3,553	34.6±2.2
44–45	44.5	2.6±0.2	32±0.08	224,640	3,438	28.5±1.9
45–46	45.5	2.2±0.1	32±0.08	224,640	4,240	30±2.1
46–47	46.5	1.8±0.1	32±0.08	224,640	4,190	25.3±1.6
47–48	47.5	1.5±0.1	32±0.08	224,640	4,172	21.5±1.4
48–49	48.5	1.3±0.1	32±0.08	224,640	4,039	17.7±1.2
49–50	49.5	1.1±0.1	32±0.08	224,640	4,623	17.3±1.1
50–51	50.5	0.9±0.1	32±0.08	224,640	4,358	13.9±0.9
51–52	51.5	0.7±0.04	32±0.08	224,640	3,532	9.6±0.6
52–53	52.5	0.6±0.04	32±0.08	224,640	3,349	7.7±0.5
53–54	53.5	0.5±0.03	32±0.08	224,640	3,840	7.5±0.5
54–55	54.5	0.4±0.02	32±0.08	224,640	4,493	7.5±0.5
Entire cross-section					170,500	**62,800±4,080**

h: Mean water depth in the cross-shore profile within the range of water depth. C_a: Depth-time-averaged SSC [The measured SSC values at the Stations A (7-m depth) and B (20-m depth) were directly used. The SSC values at other depths were predictions using an equation modified from the regression relationship in Fig. S6. The aim of this modification is to minimize the differences between the predictions and the measurements at Stations A and B. In doing so, we slightly modified the predictions at depths except for 7 and 20 m. After the modification, the correlation was changed from $C_a = 8.113e^{-0.181h}$, $R^2 = 0.99$ (Fig. S6), to $C_a = 7.706e^{-0.180h}$, $R^2 = 0.999$). V_a: Depth-time-averaged southward flow velocity (Phase 3 in Table S5). T: Storm duration. L: Length of cross-shore profile within the range of water depth (based on Fig. S1c). T_s: Amount of longshore sediment transport across the cross-shore profile within the range of water depth. $T_s = h \times C \times V \times T \times L$. The total longshore sediment transport from the delta during the storm event is the sum of individual values of T_s. kt: 1,000 tons. Notes for the uncertainty ranges are shown in Table S5.

Table S7 Annual net southward wind component and estimate of annual net southward sediment transport at the Yangtze Delta, compared with sediment discharge from the Yangtze River

	Net southward wind component (10^6 m/a)		Storm-induced southward sediment transport (Mt/a)			Nonstorm wind-induced southward sediment transport (Mt/a)			Total southward sediment transport (Mt/a)			Yangtze sediment discharge (Mt/a)
	Storm wind	Nonstorm wind	Low estimate	High estimate	Optimal estimate	Low estimate	High estimate	Optimal estimate	Low estimate	High estimate	Optimal estimate	
1979	19.1	17.3	257±17	308±21	282±55	47±3.2	93±6.3	70±37	303±21	401±27	352±93	451
1980	13.0	37.1	175±12	210±14	192±38	100±6.8	199±14	150±80	274±19	409±28	342±119	475
1981	15.9	27.3	214±15	256±17	235±46	73±5.0	147±10	110±60	287±20	403±27	345±105	535
1982	11.6	31	156±11	187±13	172±34	83±5.6	167±11	125±68	239±16	354±24	297±102	467
1983	13.5	40.1	181±12	218±15	200±40	108±7.3	216±15	162±87	289±20	433±29	361±126	499
1984	15.3	39.2	206±14	247±17	226±44	105±7.1	211±14	158±86	311±21	458±31	384±130	503
1985	7.7	30.5	103±7.0	124±8.4	114±23	82±5.6	164±11	123±66	185±13	288±20	237±89	392
1986	13.2	31.3	177±12	213±15	195±39	84±5.7	168±11	126±68	262±18	381±26	321±106	313
1987	17.3	19	233±16	279±19	256±50	51±3.5	102±6.9	77±41	284±19	381±26	332±91	404
1988	12.9	52.7	173±12	208±14	191±38	142±9.7	283±19	213±114	315±21	491±33	403±152	353
1989	10.7	51.4	144±10	173±12	158±31	138±9.4	276±19	207±112	282±19	449±31	365±143	392
1990	13.2	13.7	177±12	213±14	195±39	37±2.5	74±5.0	55±30	214±15	287±20	250±69	393
1991	8.4	51.8	113±7.7	135±9.2	124±24	139±9.5	278±19	209±112	252±17	414±28	333±137	420
1992	9.2	34.5	124±8.4	148±10	136±26	93±6.3	185±13	139±75	216±15	334±23	275±102	313
1993	14.0	36.7	188±13	226±15	207±41	99±6.7	197±13	148±79	287±20	423±29	355±120	365
1994	7.3	24.5	98±6.7	118±8.0	108±22	66±4.5	132±9.0	99±53	164±11	249±17	207±74	242
1995	1.7	21.4	23±1.6	27±1.8	25±4.5	58±3.9	115±7.8	86±46	80±5.4	142±10	111±51	353
1996	11.7	22.8	157±11	189±13	173±34	61±4.1	123±8.4	92±50	219±15	311±21	265±83	322
1997	6.2	22.7	83±5.6	100±6.8	92±18	61±4.1	122±8.3	92±49	144±9.8	222±15	183±68	298
1998	10.8	23.4	145±9.9	174±12	160±31	63±4.3	126±8.6	94±51	208±14	300±20	254±82	397
1999	14.8	28.7	199±14	239±16	219±43	77±5.2	154±10	116±62	276±19	393±27	335±106	318
2000	14.5	22.3	199±14	234±16	217±40	60±4.1	120±8.2	90±49	259±18	354±24	307±88	338
2001	13.7	33	184±13	221±15	203±40	89±6.1	177±12	133±71	273±19	398±27	336±111	278
2002	10.0	25.6	134±9.1	161±11	148±29	69±4.7	138±9.4	103±56	203±14	299±20	251±85	274
2003	12.4	29.2	167±11	200±14	183±36	78±5.3	157±11	118±64	245±17	357±24	301±100	206
2004	14.5	16.5	195±13	234±16	214±42	44±3.0	89±6.1	67±36	239±16	323±22	281±79	147
2005	6.5	15.3	87±5.9	105±7.1	96±19	41±2.8	82±5.6	62±33	128±8.7	187±13	158±52	216
2006	5.7	25.6	77±5.2	92±6.3	84±16	69±4.7	138±9.4	103±56	145±9.9	230±16	188±73	85
2007	8.4	24.3	113±7.7	135±9.2	124±24	65±4.4	131±8.9	98±53	178±12	266±18	222±77	138
2008	8.0	21.6	108±7.3	129±8.8	118±23	58±3.9	116±7.9	87±47	166±11	245±17	205±70	130
2009	11.1	17.5	149±10	179±12	164±32	47±3.2	94±6.4	71±38	196±13	273±19	235±70	111
2010	18.3	6	246±17	295±20	271±53	16±1.1	32±2.2	24±13	262±18	327±22	295±66	185
2011	10.8	34.1	145±10	174±12	160±31	92±6.3	183±12	138±74	237±16	358±24	297±106	72
2012	13.7	30.6	184±13	221±15	203±40	82±5.6	165±11	123±67	266±18	385±26	326±106	161
2013	14.9	9	200±14	240±16	220±43	24±1.6	48±3.3	36±19	224±15	289±20	257±63	117
2014	13.6	26.2	183±12	219±15	201±39	70±4.8	141±9.6	106±57	253±17	360±24	307±97	120
2015	7.7	26	103±7.0	124±8.4	114±23	70±4.8	140±9.5	105±57	173±12	264±18	219±79	116
2016	19.4	8.5	250±17	300±20	275±54	23±1.6	46±3.1	34±19	273±19	346±24	309±73	152
2017	13.1	13.5	176±12	211±14	194±38	36±2.4	73±5.0	54±30	212±14	284±19	248±68	104
2018	11.8	11.3	159±11	190±13	174±34	30±2.0	61±4.1	46±25	189±13	251±17	220±59	83
Mean±ur	**11.8±3.8**	**26.3±11**	**159±62**	**191±74**	**175±70**	**71±35**	**142±70**	**106±67**	**230±70**	**332±101**	**281±85**	**281±139**

Note: Net southward wind component is the difference between southward and northward wind components shown in Table S1. The estimate of storm-induced southward sediment transport in 2016 (i.e., 250–300 Mt/a) and the 3–5 times increase in SSC due to storm impacts (after excluding tidal effects; Fig. S3; Table S3; Reference 8) were used in the calculation of the southward sediment transport. Specifically, the low estimate of storm-induced southward sediment transport in a certain year was calculated as: $E_l = W_s/18.6*250$ here and similarly below, where E_l represents the low estimate of sediment transport, W_s represents the southward component of storm winds in the target year, 18.6 (10^6 m/a) is the southward component of storm winds in 2016, and 250 (Mt/a) is the low estimate of storm-induced southward sediment transport in 2016. The high estimate of storm-induced southward sediment transport in a certain year was calculated as: $E_h = W_s/18.6*300$, where E_h represents the high estimate of sediment transport, and 300 is the high estimate of storm-induced southward sediment transport in 2016. The low estimate of nonstorm wind-induced southward sediment transport in a certain year was calculated as: $E_l = W_{ns}/18.6*250/5$, where W_{ns} represents the southward component of nonstorm winds in the target year, and the "5" indicates that the SSC under storm conditions is 5 times greater than that under nonstorm conditions. The high estimate of nonstorm wind-induced southward sediment transport in a certain year was calculated as: $E_h = W_{ns}/18.6*300/3$, where the "3" indicates that the SSC under storm conditions is 3 times greater than that under nonstorm conditions. Optimal estimate is the average of low and high estimates. Mean±ur: mean±uncertainty range. In columns 2, 3 and 13, the uncertainty range represents the standard deviation alone. In columns 2–12, the uncertainty range represents the sum of a standard deviation and a combined error of the measurement and calculation of flow velocity, turbidity, SSC and sediment transport (see the notes for Table S5 for reference). For example, 85 in the mean±ur (281±85) of Column 12 gives a standard deviation 66 (from the average of 281) and a combined error of measurement and calculation of 19.

Table S8 Seasonal contributions to the total annual net southward storm wind component suggesting seasonal changes in storm-induced southward sediment transport.

	Annual (10^6 m/a)	Winter quarter (10^6 m)	Spring quarter (10^6 m)	Summer quarter (10^6 m)	Autumn quarter (10^6 m)	Winter half (10^6 m)	Summer half (10^6 m)
1979	19.1	5.7	0.6	1.0	11.9	13.8	5.3
1980	13.0	8.4	0.5	-0.2	4.3	11.3	1.7
1981	15.9	5.5	0.3	0.6	9,5	11.9	4.0
1982	11.6	6.3	3.2	-0.3	2.4	11.8	-0.2
1983	13.5	5.1	1.1	0.7	6.5	7.6	5.9
1984	15.3	11.0	1.4	1.2	1.7	14.3	1.0
1985	7.7	6.3	0.9	-3.2	3.7	9.1	-1.4
1986	13.2	5.6	0.8	2.2	4.7	9.3	3.9
1987	17.3	10.7	1.9	-1.0	5.6	18.3	-1.0
1988	12.9	5.6	1.2	0.5	5.7	11.9	1.0
1989	10.7	2.9	1.6	-0.7	6.9	10.6	0.1
1990	13.2	7.8	-0.2	-1.8	7.2	12.6	0.6
1991	8.4	5.1	0.3	-0.2	3.2	7.5	0.7
1992	9.2	3.6	2.3	-1.0	4.4	8.6	0.7
1993	14.0	10.5	0.7	-0.1	2.9	13.9	0.2
1994	7.3	5.4	0.6	-2.0	3.3	8.6	-1.3
1995	1.7	2.8	-0.3	-4.6	3.9	6.2	-4.5
1996	11.7	7.3	-0.1	-1.7	6.2	9.4	2.3
1997	6.2	6.3	0.0	-3.6	3.4	8.1	-1.9
1998	10.8	7.1	0.7	-1.4	4.4	9.3	1.5
1999	14.8	6.1	2.0	-0.6	7.4	10.7	4.1
2000	14.5	6.1	0.5	-2.7	9.3	11.1	3.4
2001	13.7	9.0	1.3	-0.6	4.0	12.4	1.3
2002	10.0	6.5	-1.1	0.6	3.9	7.9	2.1
2003	12.4	5.8	2.6	0.0	4.0	9.5	2.9
2004	14.5	7.4	2.8	-1.5	5.7	12.0	2.4
2005	6.5	6.6	1.5	-2.6	1.0	8.7	-2.2
2006	5.7	3.9	0.8	-2.4	3.4	6.1	-0.4
2007	8.4	4.3	3.1	-0.6	1.6	7.9	0.5
2008	8.0	6.6	0.7	-2.6	3.3	9.3	-0.8
2009	11.1	5.0	0.4	-0.1	5.8	11.0	0.1
2010	18.3	10.3	2.7	-0.2	5.5	18.2	0.1
2011	10.8	6.2	-1.1	0.9	4.9	9.6	1.2
2012	13.7	8.1	-0.1	1.0	4.7	11.1	2.6
2013	14.9	5.8	4.1	-2.9	7.9	13.8	1.0
2014	13.6	8.0	0.4	1.0	4.2	10.6	3.0
2015	7.7	3.8	1.4	0.4	2.1	6.6	1.0
2016	**18.6**	**6.5**	**4.0**	**1.1**	**7.0**	**13.7**	**4.9**
2017	13.1	4.5	0.2	-0.1	8.5	9.8	3.3
2018	11.8	7.8	2.4	-1.6	3.1	10.9	0.9
Mean±std	11.8±3.8	6.5±2.1	1.1±1.2	-0.7±1.5	4.9±2.3	10.6±3.0	1.3±2.2

Winter quarter: December to February. Spring quarter: March to May. Summer quarter: June to August. Autumn quarter: September to November. Winter half: 16 October to 15 April. Summer half: 16 April to 15 October. Negative values indicate that northward component is larger than southward component.